Geophysical Journal International

Geophys. J. Int. (2018) **215,** 1410–1426
Advance Access publication 2018 August 09
GJI Seismology

doi: 10.1093/gji/ggy331

Crustal structure surrounding the northern Malawi rift and beneath the Rungwe Volcanic Province, East Africa

David Borrego,[1] Andrew A. Nyblade,[1] Natalie J. Accardo,[2] James B. Gaherty,[2] Cynthia J. Ebinger,[3] Donna J. Shillington,[2] Patrick R.N. Chindandali,[4] Gabriel Mbogoni,[5] Richard Wambura Ferdinand,[6] Gabriel Mulibo[6], J.P. O'Donnell,[1] Marsella Kachingwe[1] and Gabrielle Tepp[5,7]

[1]*Department of Geosciences, The Pennsylvania State University, State College, PA, USA. E-mail: aan2@psu.edu*
[2]*Lamont-Doherty Earth Observatory of Columbia University, Palisades, New York, NY, USA*
[3]*Department of Earth and Environmental Sciences, Tulane University, New Orleans, LA, USA*
[4]*Geological Survey of Malawi, Zomba, Malawi*
[5]*Geological Survey of Tanzania, Dodoma, Tanzania*
[6]*University of Dar-es-Salaam, Dar-es-Salaam, Tanzania*
[7]*Department of Physics & Astronomy, University of Rochester, Rochester, NY, USA*

Accepted 2018 August 8. Received 2018 August 3; in original form 2018 January 30

SUMMARY

The crustal structure surrounding the northern Malawi rift and beneath the Rungwe Volcanic Province (RVP) has been investigated using teleseismic earthquakes recorded on SEGMeNT broad-band seismic stations to determine the extent to which the crust has been modified by Cenozoic rifting and magmatism. The SEGMeNT network included 57 broad-band seismic stations deployed in northern Malawi and southern Tanzania between August 2013 and October 2015. Estimates of crustal thickness, shear wave velocity and Poisson's ratio have been obtained by modelling *P*-wave receiver functions using the *H–k* stacking method and jointly inverting receiver functions with Rayleigh wave phase velocities. These estimates are used to investigate the extent of magmatic modification to the crust, indicated by changes in Poisson's ratio, and the geometry of crustal thinning along the northern margins of the Malawi rift and beneath the RVP. The average crustal thickness for the four stations in the RVP is 39 km, the average Poisson's ratio is 0.28 ($Vp/Vs = 1.83$), and the average crustal shear wave velocity is 3.6 km s^{-1}. Although the RVP has been a site of ongoing magmatism since at least 17 Ma and is associated with a pronounced low velocity zone in the mantle, our results show little evidence that the bulk composition or thickness of the crust beneath the RVP has been significantly modified by magmatism or extension. However, Poisson's ratios of 0.29–0.31 ($Vp/Vs = 1.85$–1.91) at three of the stations in the RVP, where there is also no evidence for higher Vs, may indicate the presence of partial melt in the crust. The average crustal thickness of Proterozoic terranes surrounding the northern end of the Malawi rift ranges from 38 to 42 km. For most of the terranes, average Poisson's ratios are between 0.25 and 0.26 ($Vp/Vs = 1.73$–1.76), with the exception of the Irumide Belt, which has an average Poisson's ratio of 0.23 ($Vp/Vs = 1.68$). The average crustal shear wave velocities for all the terranes are either 3.6 or 3.7 km s^{-1}. These results indicate a bulk felsic to intermediate crustal composition for all terranes, consistent with previous results, and reveal that there is little, if any, crustal thinning beneath the uplifted flanks of asymmetric basins within the northern Malawi rift or beneath the RVP. Consequently, crustal thinning in the northern Malawi rift must be highly focused beneath the centres of rift basin segments, consistent with models of rift flank topography and gravity observations.

Key words: Composition and structure of the continental crust; Africa; Continental tectonics: extensional.

Downloaded from https://academic.oup.com/gji/article-abstract/215/2/1410/5068696 by Penn State University (Paterno Lib) user on 17 September 2018

© The Author(s) 2018. Published by Oxford University Press on behalf of The Royal Astronomical Society.

1 INTRODUCTION

Continental rifting processes involve lithospheric stretching with or without the production of magma from adiabatic decompression melting. The crustal stretching is highly segmented, potentially giving rise to significant across- and along-axis variations in crustal thickness and magmatic modification (e.g. Ebinger *et al.* 1989; Shillington *et al.* 2016). In this study, crustal structure surrounding the northern half of the Malawi rift in eastern Africa has been investigated to determine the extent to which the crust has been modified by Cenozoic rifting and magmatism. The Malawi rift, which is part of the Western branch of the East African rift system, developed within a number of Proterozoic mobile belts south of the Tanzania Craton and east of the Bangweulu Craton (Fig. 1). At its northern end, volcanoes of the Cenozoic Rungwe Volcanic Province (RVP) rise some 2300 m above Lake Malawi (Nyasa; Fig. 1). Using broad-band seismic data from 57 seismic stations deployed as part of the Study of Extension and maGmatism in Malawi and Tanzania (SEGMeNT) project (Shillington *et al.* 2016), estimates of crustal thickness, shear wave velocity structure, and Poisson's ratio (*Vp*/*Vs*) are reported. Attempts to determine crustal thickness using receiver function techniques from lake-bottom seismometer data were compromised by reverberations in the 3–5-km-thick, low-velocity sedimentary sequences.

These estimates are used to investigate the extent of magmatic modification to the crust, indicated by changes in Poisson's ratio and thinning to the crust along the northern margins of the Malawi rift and beneath the RVP, indicated by changes in crustal thickness. Understanding how magmatism may have modified the Proterozoic crust in the Western branch is important for constraining the distribution and volume of Cenozoic magmatism and addressing the role of magmatism in the early stages of rift development (e.g. Buck 2004; Casey *et al.* 2006). In the Western branch, surface expressions of magmatism are confined to five volcanic provinces (e.g. Furman 2007), and some of these appear to be underlain by relatively localized mantle low-velocity anomalies (e.g. Adams *et al.* 2012; Jakovlev *et al.* 2013; O'Donnell *et al.* 2013), but the volume and distribution of magmatic addition to the crust and its relationship to extension is poorly known. Recent studies of some magmatic segments of the East African rift system suggest that magmatic underplating and stretching may be localized to the fault bounded rift valley, as evidenced by an outward-dipping and gradational Moho and high crustal Poisson's ratios (Wölbern *et al.* 2010; Gummert *et al.* 2015; Hodgson *et al.* 2017; Plasman *et al.* 2017).

Understanding the amount and location of crustal thinning beneath and surrounding the Malawi rift is also important for evaluating models of crustal extension and identifying where strain is being localized during the rifting process. Competing models for extension make different predictions for the distribution of stretching throughout the crust and mantle lithosphere (e.g. Burov & Poliakov 2001; Van Wijk *et al.* 2008; Huismans & Beaumont 2011; Brune *et al.* 2016; Olive *et al.* 2016).

Crustal structure has been investigated using two methods, *H–k* stacking of *P*-wave receiver functions (Zhu & Kanamori 2000) and a joint inversion of *P*-wave receiver functions and Rayleigh wave phase velocities (Julià *et al.*, 2000, 2003). Results from applying these methods to the SEGMeNT data have been combined with results from previous studies in eastern Africa to examine crustal structure across the study area and identify the nature of crustal modification, if any, which may have resulted from Cenozoic rifting and magmatism.

2 GEOLOGY

The study area is located at the southern end of the Western rift, one arm of the East African rift system (Fig. 1). The EARS is a divergent plate boundary over 4000 km long, stretching from the Afar triple junction in the north to Mozambique in the southeast, and to Botswana in the southwest. The rift system south of Ethiopia comprises at least three branches, the Eastern, Western and Southwestern rifts, which have mainly developed in Proterozoic mobile belts surrounding Archean cratons (McConnell 1972).

The study area includes the RVP and the Precambrian terranes that underlay the RVP and surround the northern portion of the Malawi rift (Fig. 1). The Malawi rift is part of the Western branch of the EARS, and extends for ∼800 km from the RVP in the north to the Urema Graben in the south. The majority of the rift is occupied by the ∼40–60 km wide Lake Malawi (Nyasa), and consists of several half-grabens bounded by border faults (e.g. Ebinger *et al.* 1989; Specht & Rosendahl 1989) with up to 5 km of synrift sediment (Accardo *et al.* in review). Parts of the Western rift may have initiated as early as 26 Ma (Roberts *et al.* 2012), but volcanism in the RVP initiated *ca*. 17 Ma (Rasskazov *et al.* 2003; Mesko *et al.* 2014). The RVP lies within a complex accommodation zone between the Rukwa, Malawi and Usangu rifts, and includes three stratovolcanoes that have experienced Plinian and basaltic eruptions in the past 10 Ka: Ngozi, Rungwe and Kyejo (Ebinger *et al.* 1989; Fontijn *et al.* 2010a, b, 2012; Fig. 1). The most common lavas within the RVP are basalts, trachytes and phonolites (e.g. Fontijn *et al.* 2010a, b).

The Precambrian tectonic framework of the study region includes the Archean Tanzania Craton, just to the north of the RVP, and several Proterozoic mobile (orogenic) belts beneath and surrounding the RVP and Malawi rift (Fig. 1). The Usagaran Belt consists predominately of granitoids and orthogneisses that were derived from reworking and recycling of the Tanzania Craton (Cahen & Snelling 1983; Schlüter & Hampton 1997; de Waele *et al.* 2008). The Ubendian Belt consists mostly of granulite and amphibolite facies gneisses and metasedimentary rocks that formed during two orogenic events between 2.03 and 1.86 Ga, resulting in granitoid intrusions and exhumation of granulities and eclogites (Cahen & Snelling 1983; Lenoir *et al.* 1994; Schlüter & Hampton 1997). The Irumide Belt consists of reworked Archean and Paleoproterozoic crust overlain by ∼2 Ga rhyolites and sediments (Begg *et al.* 2009). During the Irumide orogeny ∼1 Ga, the crust was strongly deformed by isoclinal folding and thrusting, resulting in crustal thickening with some addition of juvenile crust (De Waele *et al.* 2006). The Mozambique Belt consists of gneisses and granulites and formed from multiple collision events between 1200 and 450 Ma (Cahen & Snelling 1983; Fritz *et al.* 2013).

Throughout the study area there are isolated outcrops of Late Carboniferous–Early Jurassic (Karoo) sedimentary strata originally deposited in rift basins, including the Ruhuhu basin that crosses the Malawi rift (Fig. 1). The Karoo rifts formed during the break up of Gondwana (Cox 1970). The characteristically red sandstones of the Karoo have been eroded and redeposited in Cretaceous, Palaeogene and recent rifts, leading to reclassifications (e.g. Roberts *et al.* 2010, 2012). Karoo sediments also appear to underlie parts of the northern Malawi rift (Accardo *et al.* in review).

3 PREVIOUS CRUSTAL STUDIES

A number of previous studies have reported estimates of Moho depth, Poisson's ratio and *Vs* for the Precambrian terranes in the study area by modelling a combination of teleseismic receiver

Downloaded from https://academic.oup.com/gji/article-abstract/215/2/1410/5068696 by Penn State University (Paterno Lib) user on 17 September 2018

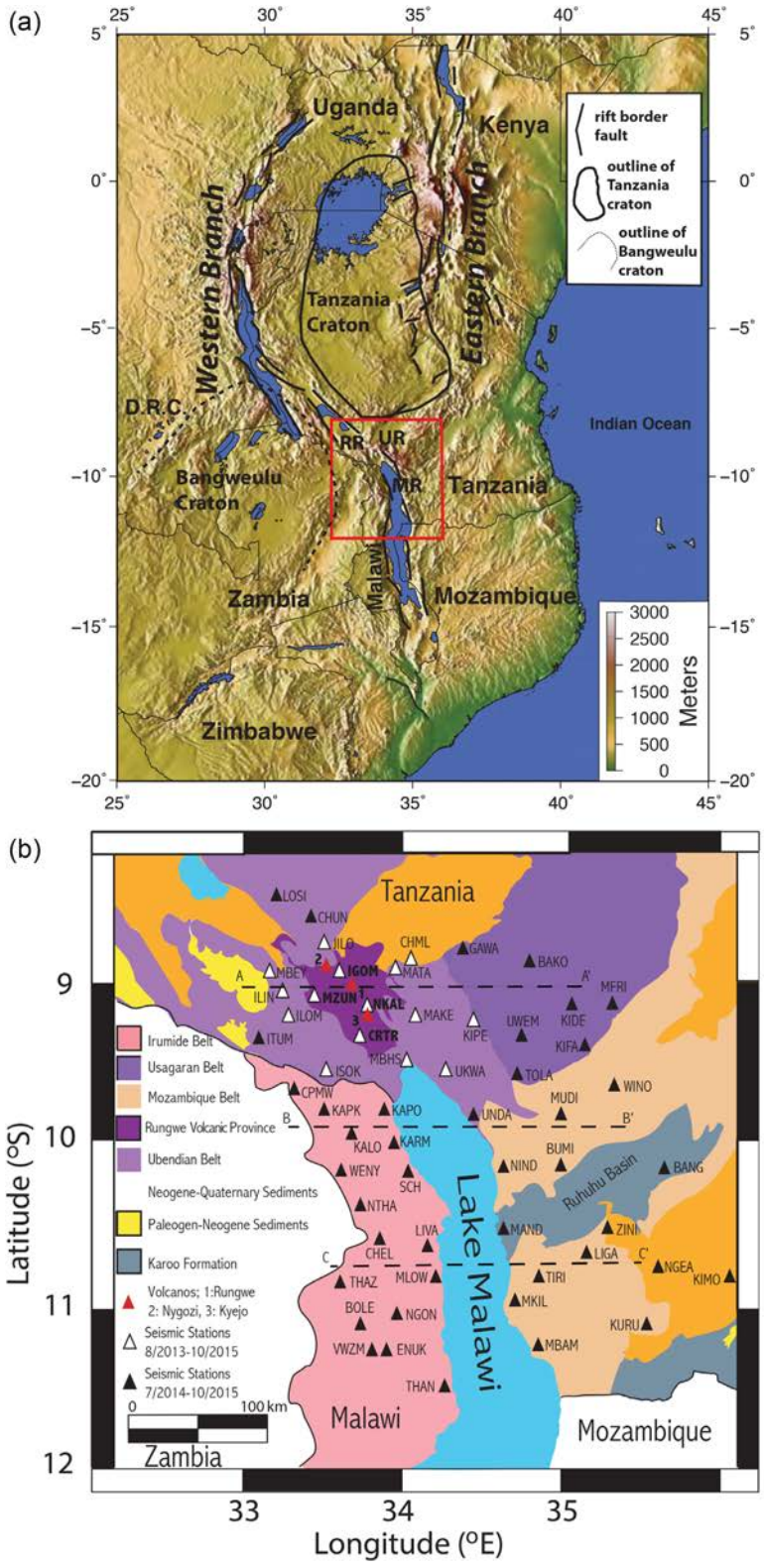


Figure 1. (a) Topographic map of eastern Africa showing craton boundaries and major rift faults. The red box shows the area in (b). RR, Rukwa Rift; UR, Usgangu Rift; MR, Malawi Rift. (b) Map showing the geology of the study area and the locations of the SEGMeNT project seismic stations. The map is modified from Mulibo & Nyblade (2016).

Downloaded from https://academic.oup.com/gji/article-abstract/215/2/1410/5068696 by Penn State University (Paterno Lib) user on 17 September 2018

Table 1. Crustal structure results.

Tectonic region	Station name	Rfs	Lat. (°)	Long. (°)	Elev. (m)	H (1) (km)	k (1)	JI (km)	Avg Vs (km s^{-1})	Mafic lower crust (km)	Poisson's ratio	Ps ± S.D. (km)	H, k (2) (km)	H, k (3) (km)	Q	S
Rungwe Volcanics	CRTR	6	−9.33	33.75	916	45.5 ± 2.8	1.85 ± 0.10	45.0	3.6	0.0	0.29 ± 0.03	47 ± 6.3	43.9, 1.86	47.7, 1.85	C	1
	IGOM	7	−9.00	33.66	2364	33.6 ± 1.3	1.91 ± 0.09	35.0	3.6	5.0	0.31 ± 0.03	36 ± 5.0	32.3, 1.92	35.5, 1.90	C	1
	MZUN	14	−9.15	33.52	1399	39.0 ± 2.4	1.67 ± 0.05	35.0	3.6	5.0	0.22 ± 0.03	34 ± 2.4	37.5, 1.68	41.2, 1.66	B	1
	NKAL	9	−9.19	33.77	1551	34.6 ± 1.2	1.88 ± 0.05	35.0	3.6	5.0	0.30 ± 0.02	40 ± 2.9	33.3, 1.89	36.6, 1.87	B	1
	Average1					**39**	**1.83**		**3.6**		**0.28**					
Ubendian Belt	∗CHUN	6	−8.54	33.43	1527	37.0 ± 1.9	1.71 ± 0.08	35.0	3.6	0.0	0.24 ± 0.04	34 ± 4.5	35.7, 1.72	39.0, 1.71	C	1
	ILIN	21	−9.08	33.33	1919	40.1 ± 1.5	1.74 ± 0.04	37.5	3.5	0.0	0.25 ± 0.02	39 ± 2.4	38.6, 1.75	42.5, 1.73	A	1
	∗ILOM	15	−9.28	33.34	2110	39.0 ± 3.1	1.76 ± 0.15	37.5	3.6	0.0	0.26 ± 0.06	35 ± 6.8	37.5, 1.76	41.2, 1.74	C	1
	ISOK	14	−9.51	33.49	1443	43.5 ± 1.3	1.61 ± 0.03	40.0	3.6	0.0	0.19 ± 0.03	35 ± 2.2	41.8, 1.62	46.0, 1.60	B	1
	ITUM	13	−9.40	33.19	1365	38.9 ± 0.7	1.80 ± 0.03	37.5	3.6	0.0	0.28 ± 0.02	40 ± 2.1	37.5, 1.81	41.2, 1.78	A	1
	JILO	21	−8.73	33.57	2002	37.9 ± 1.2	1.74 ± 0.03	37.5	3.6	0.0	0.25 ± 0.01	37 ± 5.7	36.5, 1.80	40.1, 1.78	A	1
	LOSI	8	−8.39	33.17	1233	36.8 ± 3.3	1.79 ± 0.13	37.5	3.6	0.0	0.27 ± 0.06	34 ± 4.3	35.4, 1.75	38.8, 1.73	C	1
	∗MAKE	14	−9.26	34.10	2304	48.0 ± 3.5	1.71 ± 0.05	47.5	3.8	7.5	0.24 ± 0.02	45 ± 2.1	46.3, 1.72	50.8, 1.70	B	1
	MATA	11	−8.96	33.97	2074	40.4 ± 1.4	1.77 ± 0.06	42.5	3.7	7.5	0.27 ± 0.02	41 ± 2.8	39.0, 1.77	42.7, 1.75	A	1
	MBEYA	25	−9.00	33.25	1393	40.8 ± 2.3	1.71 ± 0.04	40.0	3.6	2.5	0.24 ± 0.02	38 ± 2.5	39.3, 1.72	43.0, 1.70	A	1
	MBHS	9	−9.43	33.98	560	38.8 ± 3.4	1.77 ± 0.08	40.0	3.6	5.0	0.27 ± 0.04	37 ± 1.6	37.4, 1.78	41.0, 1.76	A	1
	UKWA	17	−9.45	34.22	2143	49.4 ± 4.4	1.76 ± 0.07	47.5	3.8	7.5	0.26 ± 0.03	46 ± 5.6	47.6, 1.76	52.2, 1.75	C	1
	UNDA	10	−9.85	34.47	1767	43.4 ± 2.4	1.66 ± 0.07	42.5	3.7	7.5	0.22 ± 0.04	38 ± 3.9	41.8, 1.67	45.8, 1.66	B	1
	Average1					**41**	**1.73**		**3.6**		**0.25**					
	$MBEY_A$	–	−9.00	33.25	1331	40.1 ± 3.6	1.69 ± 0.07	37.5	3.6	0.0	0.23 ± 0.03	–	–	–	–	2
	UVZA	16	−5.10	30.39	992	39.0 ± 0.9	1.80 ± 0.04	41.0	3.7	3.0	0.28 ± 0.02	–	–	–	–	2
	INZA	–	−5.12	30.40	975	–	–	–	–	–	–	42	–	–	–	2
	PNDA	26	−6.25	31.06	1071	40.9 ± 1.3	1.82 ± 0.05	38.0	3.6	0.0	0.28 ± 0.02	–	–	–	–	2
	NAMA	20	−7.51	31.04	1559	47.5 ± 2.1	1.70 ± 0.05	46.0	3.8	8.0	0.24 ± 0.02	–	–	–	–	2
	LAEL	11	−8.57	32.06	1596	46.7 ± 1.1	1.72 ± 0.03	43.0	3.7	3.0	0.24 ± 0.01	–	–	–	–	2
	LOSS	12	−8.42	33.16	1195	49.2 ± 2.0	1.79 ± 0.03	51.0	3.8	15.0	0.27 ± 0.01	–	–	–	–	2
	TUND	7	−9.30	32.77	1697	43.8 ± 1.9	1.77 ± 0.05	45.0	3.7	5.0	0.27 ± 0.02	–	–	–	–	2
	PAND	–	−8.98	33.24	1248	35	1.72	43.0	3.7	5.0	0.24	–	–	–	–	2
	GOMA	–	−4.84	29.70	880	44	1.74	45.0	3.6	3.0	0.25	–	–	–	–	2
	KGMA	19	−4.88	29.63	821	39.6 ± 1.7	1.81 ± 0.17	41.0	3.7	0.0	0.28 ± 0.06	–	–	–	–	2
	SUMB	–	−7.95	31.62	1837	–	–	46.0	–	–	–	45	–	–	–	2
	Average2					**42**	**1.74**		**3.7**		**0.25**					
Usagaran Belt	BAKOD	6	−8.84	34.80	1651	36.0 ± 2.5	1.79 ± 0.08	37.5	3.7	5.0	0.27 ± 0.04	40 ± 4.2	34.6, 1.80	38.2, 1.78	B	1
	^ CHMLE	9	−8.83	34.03	1118	33.5 ± 1.4	1.80 ± 0.10	–	–	–	0.28 ± 0.04	36 ± 2.0	32.3, 1.81	35.4, 1.79	B	1
	GAWA	15	−8.76	34.39	1127	36.7 ± 1.7	1.77 ± 0.06	37.5	3.7	2.5	0.27 ± 0.03	37 ± 2.5	35.4, 1.77	38.9, 1.75	A	1
	∗KIDE	7	−9.27	35.02	1760	34.5 ± 2.6	1.66 ± 0.08	32.5	3.7	5.0	0.22 ± 0.05	29 ± 2.0	33.1, 1.67	36.8, 1.64	B	1
	∗KIFA	6	−9.55	35.10	1742	37.9 ± 1.6	1.64 ± 0.07	35.0	3.7	10.0	0.20 ± 0.05	33 ± 2.8	36.4, 1.65	40.1, 1.63	B	1
	KIPE	21	−9.29	34.44	2224	42.2 ± 3.4	1.63 ± 0.06	42.5	3.8	10.0	0.20 ± 0.05	36 ± 2.2	40.3, 1.65	44.6, 1.62	A	1
	MFRI	11	−9.29	35.31	1604	30.6 ± 2.2	1.77 ± 0.10	32.5	3.6	2.5	0.27 ± 0.04	32 ± 1.9	29.5, 1.78	32.4, 1.76	B	1
	TOLA	8	−9.59	34.58	2201	43.7 ± 1.5	1.89 ± 0.05	47.5	3.8	15.0	0.31 ± 0.02	52 ± 1.3	42.1, 1.89	46.0, 1.88	A	1
	UWEM	6	−9.47	34.79	2151	37.5 ± 2.4	1.86 ± 0.09	40.0	3.8	7.5	0.30 ± 0.08	44 ± 3.5	46.9, 1.69	51.6, 1.66	B	1

Downloaded from https://academic.oup.com/gji/article-abstract/215/2/1410/5068696 by Penn State University (Paterno Lib) user on 17 September 2018

Table 1. Continued

Tectonic region	Station name	Rfs	Lat. (°)	Long. (°)	Elev. (m)	H (1) (km)	k (1)	JI (km)	Avg Vs (km s^{-1})	Mafic lower crust (km)	Poisson's ratio	Ps ± S.D. (km)	H, k (2) (km)	H, k (3) (km)	Q	S
	Average1					**38**	**1.76**		**3.7**		**0.26**					
	$MAKA_D$	7	−8.84	34.83	1685	39.1 ±2.3	1.80 ± 0.07	41.0	3.6	0.0	0.28 ± 0.03	–	–	–	–	2
	CHIME	–	−8.83	34.03	1100	–	–	–	–	–	–	38.1	–	–	–	2
	IRIN	17	−7.76	35.69	1561	39.4 ± 1.4	1.74 ± 0.04	36.0	3.7	5.0	0.25 ± 0.02	–	–	–	–	2
	MAFI	20	−8.31	35.31	1866	38.8 ± 1.4	1.74 ± 0.04	36.0	3.6	5.0	0.25 ± 0.02	–	–	–	–	2
	NJOM	9	−9.37	34.79	1949	32.3 ± 1.3	1.73 ± 0.05	33.0	–	–	0.25 ± 0.02	–	–	–	–	2
	MGOR	10	−6.83	37.67	501	36.1 ± 2.4	1.76 ± 0.09	33.0	3.5	3.0	0.26 ± 0.03	–	–	–	–	2
	MIKU	–	−7.40	36.99	518	–	–	33.0	–	–	–	37.2	–	–	–	2
	Average2					**38**	**1.76**		**3.6**		**0.26**					
Irumide Belt	BOLE	9	−10.98	33.74	1109	44.5 ± 1.0	1.65 ± 0.03	42.5	3.7	5.0	0.21 ± 0.02	39 ± 1.9	42.8, 1.66	47.0, 1.64	A	1
	CHEL	12	−10.59	33.81	2194	43.9 ± 1.2	1.72 ± 0.04	42.5	3.7	5.0	0.24 ± 0.02	42 ± 3.2	42.3, 1.73	46.3, 1.71	A	1
	CPMW	9	−9.71	33.27	1272	43.9 ± 2.7	1.66 ± 0.06	42.5	3.7	0.0	0.22 ± 0.04	37 ± 2.9	42.2, 1.67	46.3, 1.65	A	1
	ENUK	12	−11.18	33.89	1134	42.5 ± 2.1	1.69 ± 0.04	40.0	3.6	5.0	0.23 ± 0.02	39 ± 2.4	41.0, 1.70	45.0, 1.68	A	1
	KALO	4	−9.91	33.64	1065	41.5 ± 6.4	1.62 ± 0.16	35.0	3.6	2.5	0.19 ± 0.13	33 ± 3.0	40.1, 1.62	44.5, 1.59	C	1
	KAPK	12	−9.78	33.46	533	43.5 ± 3.8	1.64 ± 0.10	40.0	3.6	2.5	0.20 ± 0.06	36 ± 2.5	41.9, 1.65	45.9, 1.63	B	1
	∗KAPO	7	−9.79	33.82	527	38.4 ± 1.1	1.70 ± 0.03	35.0	3.6	5.0	0.24 ± 0.02	31 ± 3.6	37.2, 1.70	40.5, 1.69	B	1
	KARM	6	−9.95	33.90	1357	41.4 ± 2.2	1.75 ± 0.07	40.0	3.6	5.0	0.26 ± 0.03	40 ± 2.4	39.8, 1.76	43.8, 1.73	B	1
	LIVA	11	−10.61	34.11	1371	37.3 ± 1.3	1.71 ± 0.05	35.0	3.5	2.5	0.24 ± 0.03	35 ± 4.2	36.0, 1.72	39.4, 1.70	A	1
	MLOW	10	−10.78	34.21	513	40.6 ± 3.6	1.69 ± 0.05	37.5	3.5	5.0	0.23 ± 0.03	36 ± 2.3	39.0, 1.70	43.1, 1.68	B	1
	NGON	6	−10.94	33.94	1060	37.0 ± 3.7	1.69 ± 0.06	40.0	3.7	7.5	0.23 ± 0.04	35 ± 2.3	35.8, 1.69	39.0, 1.68	B	1
	NTHA	8	−10.35	33.64	1291	–	-	50.0	3.8	12.5		47 ± 2.5	–	–	D	1
	SCH	9	−10.18	34.03	529	43.3 ± 1.0	1.70 ± 0.04	40.0	3.6	2.5	0.24 ± 0.02	39 ± 1.4	41.7, 1.71	45.8, 1.63	A	1
	THAN	7	−11.47	34.18	683	43.8 ± 4.9	1.67 ± 0.07	42.5	3.7	5.0	0.22 ± 0.05	39 ± 2.4	42.5, 1.67	46.3, 1.66	B	1
	THAZ	11	−10.83	33.59	1695	43.4 ± 4.8	1.73 ± 0.09	45.0	3.8	7.5	0.25 ± 0.05	41 ± 3.5	41.9, 1.73	45.9, 1.71	B	1
	VWZM	13	−11.18	33.79	1134	42.7 ± 2.1	1.68 ± 0.03	42.5	3.7	7.5	0.23 ± 0.02	38 ± 2.1	41.1, 1.69	45.0, 1.67	A	1
	∗WENY	6	−10.16	33.56	1516	48.7 ± 2.4	1.65 ± 0.07	–	–	–	0.21 ± 0.04	42 ± 2.5	46.8, 1.66	51.4, 1.64	C	1
	Average1					**42**	**1.68**		**3.6**		**0.23**					
	KASM	19	−10.22	31.14	1386	43.0 ± 2.8	1.63 ± 0.08	40.0	3.7	2.0	0.20 ± 0.01	40	–	–	–	3
	CHAM	6	−10.95	31.07	1211	41.1 ± 0.9	1.72 ± 0.04	38.0	3.7	0.0	0.24 ± 0.01	38	–	–	–	3
	ISOK	16	−10.17	32.65	1301	44.2 ± 1.1	1.66 ± 0.04	40.0	3.7	0.0	0.22 ± 0.02	40	–	–	–	3
	KISH	6	−12.02	29.61	1132	37.8 ± 0.8	1.71 ± 0.03	38.0	3.7	3.0	0.24 ± 0.01	38	–	–	–	3
	MANS	10	−11.14	28.87	1259	41.8 ± 1.6	1.78 ± 0.05	43.0	3.8	13.0	0.27 ± 0.01	43	–	–	–	3
	MKUS	5	−13.60	29.38	1250	43.5 ± 0.9	1.64 ± 0.02	40.0	3.7	5.0	0.20 ± 0.01	40	–	–	–	3
	MPIK	11	−11.82	31.45	1392	48.2 ± 1.7	1.67 ± 0.06	45.0	3.8	7.0	0.22 ± 0.02	45	–	–	–	3
	SERJ	10	−13.23	30.21	1388	45.2 ± 1.6	1.70 ± 0.03	43.0	3.8	5.0	0.24 ± 0.02	43	–	–	–	3
	SHWG	5	−11.19	31.74	1211	45.1 ± 2.6	1.69 ± 0.09	43.0	3.7	5.0	0.23 ± 0.02	43	–	–	–	3

Downloaded from https://academic.oup.com/gji/article-abstract/215/2/1410/5068696 by Penn State University (Paterno Lib) user on 17 September 2018

Table 1. Continued

Tectonic region	Station name	Rfs	Lat. (°)	Long. (°)	Elev. (m)	H (1) (km)	k (1)	JI (km)	Avg Vs (km s^{-1})	Mafic lower crust (km)	Poisson's ratio	Ps ± S.D. (km)	H, k (2) (km)	H, k (3) (km)	Q	S
	Average3					**43**	**1.69**		**3.7**		**0.23**					
Mozambique Belt	BANG	10	−10.11	35.65	960	40.1 ± 1.8	1.77 ± 0.03	37.5	3.6	2.5	0.27 ± 0.01	37 ± 1.5	38.7, 1.78	42.2, 1.77	A	1
	BUMI	10	−10.13	34.94	1333	40.2 ± 1.7	1.77 ± 0.04	42.5	3.7	2.5	0.27 ± 0.02	41 ± 2.5	38.7, 1.78	42.4, 1.76	A	1
	KIMO	14	−10.69	36.05	841	36.5 ±0.9	1.66 ± 0.04	35.0	3.6	5.0	0.22 ± 0.03	31 ± 2.6	35.2, 1.67	38.5, 1.66	A	1
	KURU	13	−11.20	35.46	751	36.7 ± 1.2	1.71 ± 0.05	37.5	3.7	5.0	0.24 ± 0.03	34 ± 2.8	35.4, 1.72	38.9, 1.70	A	1
	LIGA	15	−10.68	35.25	976	38.3 ± 1.5	1.71 ± 0.07	37.5	3.7	2.5	0.24 ± 0.03	35 ± 4.5	36.9, 1.72	40.3, 1.71	B	1
	MAND	12	−10.48	34.60	511	36.7 ± 3.7	1.71 ± 0.06	37.5	3.6	5.0	0.24 ± 0.03	33 ± 2.5	35.3, 1.72	38.7, 1.70	B	1
	MBAM	9	−11.25	34.79	560	40.5 ± 3.4	1.72 ± 0.09	40.0	3.6	2.5	0.24 ± 0.05	37 ± 3.9	39.0, 1.73	42.7, 1.71	B	1
	MKIL	11	−10.88	34.68	490	41.5 ± 1.8	1.73 ± 0.07	40.0	3.6	2.5	0.25 ± 0.04	39 ± 5.3	39.8, 1.74	44.0, 1.71	B	1
	MUDI	11	−9.86	34.94	1397	48.7 ± 5.0	1.73 ± 0.11	45.0	3.8	10.0	0.25 ± 0.05	48 ± 3.5	47.0, 1.73	51.5, 1.71	B	1
	NGEAB	17	−10.68	35.67	1200	36.9 ± 0.9	1.72 ± 0.05	35.0	3.6	2.5	0.24 ± 0.03	34 ± 3.8	35.5, 1.73	38.9, 1.71	A	1
	NIND	7	−10.14	34.58	1292	37.1 ± 4.7	1.89 ± 0.21	40.0	3.7	10.0	0.31 ± 0.05	38 ± 1.1	35.9, 1.89	39.4, 1.87	C	1
	TIRI	6	−10.76	34.88	1295	38.3 ± 2.4	1.78 ± 0.06	40.0	3.7	5.0	0.27 ± 0.03	40 ± 2.7	36.9, 1.79	40.2, 1.77	B	1
	WINOC	14	−9.76	35.30	1486	43.0 ± 1.5	1.70 ± 0.07	40.0	3.7	7.5	0.24 ± 0.04	38 ± 4.5	41.5, 1.71	45.6, 1.69	B	1
	ZINI	15	−10.47	35.34	1044	39.0 ± 1.0	1.71 ± 0.03	37.5	3.7	2.5	0.24 ± 0.02	36 ± 1.8	37.5, 1.72	41.1, 1.70	A	1
	Average1					**40**	**1.74**		**3.7**		**0.25**					
	SONGB	17	−10.67	35.65	1119	37.0 ± 0.8	1.71 ± 0.04	36.0	3.6	3.0	0.24 ± 0.02	–	–	–	–	2
	WINOC	12	−9.76	35.30	1511	39.6 ± 2.5	1.82 ± 0.09	41.0	3.6	–	0.28 ± 0.03	–	–	–	–	2
	MAUS	31	−2.74	36.70	1334	39.1 ± 1.0	1.67 ± 0.02	38.0	3.6	3.0	0.24 ± 0.01	–	–	–	–	2
	LONG	–	−2.73	36.70	1380	37 ± 4	1.78	40.0	3.6	3.0	0.27	–	–	–	–	2
	HALE	–	−5.30	38.62	230	–	–	38.0	3.7	3.0	–	39 ± 4	–	–	–	2
	KIBA	–	−5.32	36.57	1500	–	–	40.0	3.7	5.0	–	36 ± 4	–	–	–	2
	KIBE	–	−5.38	37.48	997	37 ± 4	1.74	38.0	3.6	0.0	0.25	–	–	–	–	2
	KOMO	–	−3.84	36.72	1114	36 ± 4	1.72	38.0	3.6	0.0	0.24	–	–	–	–	2
	KOND	–	−4.90	35.80	1419	37 ± 4	1.78	35.0	3.6	0.0	0.27	–	–	–	–	2
	TARA	–	−3.89	36.01	1268	37 ± 4	1.74	40.0	3.6	3.0	0.25	–	–	–	–	2
	ANGA	–	−2.50	36.80	1000	39 ± 3.0	1.70 ± 0.07	38.0	3.6	0.0	0.24 ± 0.03	–	–	–	–	2
	KAKA	–	0.56	34.80	1477	37 ± 2.0	1.67 ± 0.07	38.0	3.6	0.0	0.24 ± 0.03	–	–	–	–	2
	KITU	–	−1.37	38.00	1129	40 ± 3.9	1.73 ± 0.07	35.0	3.6	0.0	0.25 ± 0.03	–	–	–	–	2
	KMBO	–	−1.13	37.35	1940	41 ± 2.6	1.74 ± 0.05	40.0	3.6	3.0	0.26 ± 0.02	–	–	–	–	2
	KR42	–	0.04	35.73	2157	38 ± 4.8	1.81 ± 0.16	–	–	–	0.26 ± 0.06	–	–	–	–	2
	NAI	–	−1.13	36.80	1692	42 ± 2.3	1.75 ± 0.04	–	–	–	0.26 ± 0.02	–	–	–	–	2
	TALE	–	0.98	34.98	1821	38 ± 3.2	1.76 ± 0.04	38.0	3.7	0.0	0.27 ± 0.02	–	–	–	–	2
	Average2					**39**	**1.74**		**3.6**		**0.25**					

rf = number of RFs, H = Crustal Thickness, k = Vp/Vs ratio, JI = H from Joint Inversion, Ps = H from Moho Ps time, Q = Qualitative grade, H, k (1): H from H–k stacking; ave. Vp = 6.5 km s^{-1}, H, k (2): ave. Vp = 6.3 km s^{-1}, H, k (3): ave. Vp = 6.8 km s^{-1}, Average1 = average for this study, Average2 = average for both 1 and 2 Source, Average3 = average for both 1 and 3 Source, S = Source. 1 = This study; 2 = Tugume *et al.* (2012); 3 = Kachingwe *et al.* (2015)., Subscripts A, B, C, D, E = indicates stations at same locations.

∗ = RFs computed using Gaussian of 2.5.

^ = RFs computed using Gaussian of 0.5.

Downloaded from https://academic.oup.com/gji/article-abstract/215/2/1410/5068696 by Penn State University (Paterno Lib) user on 17 September 2018

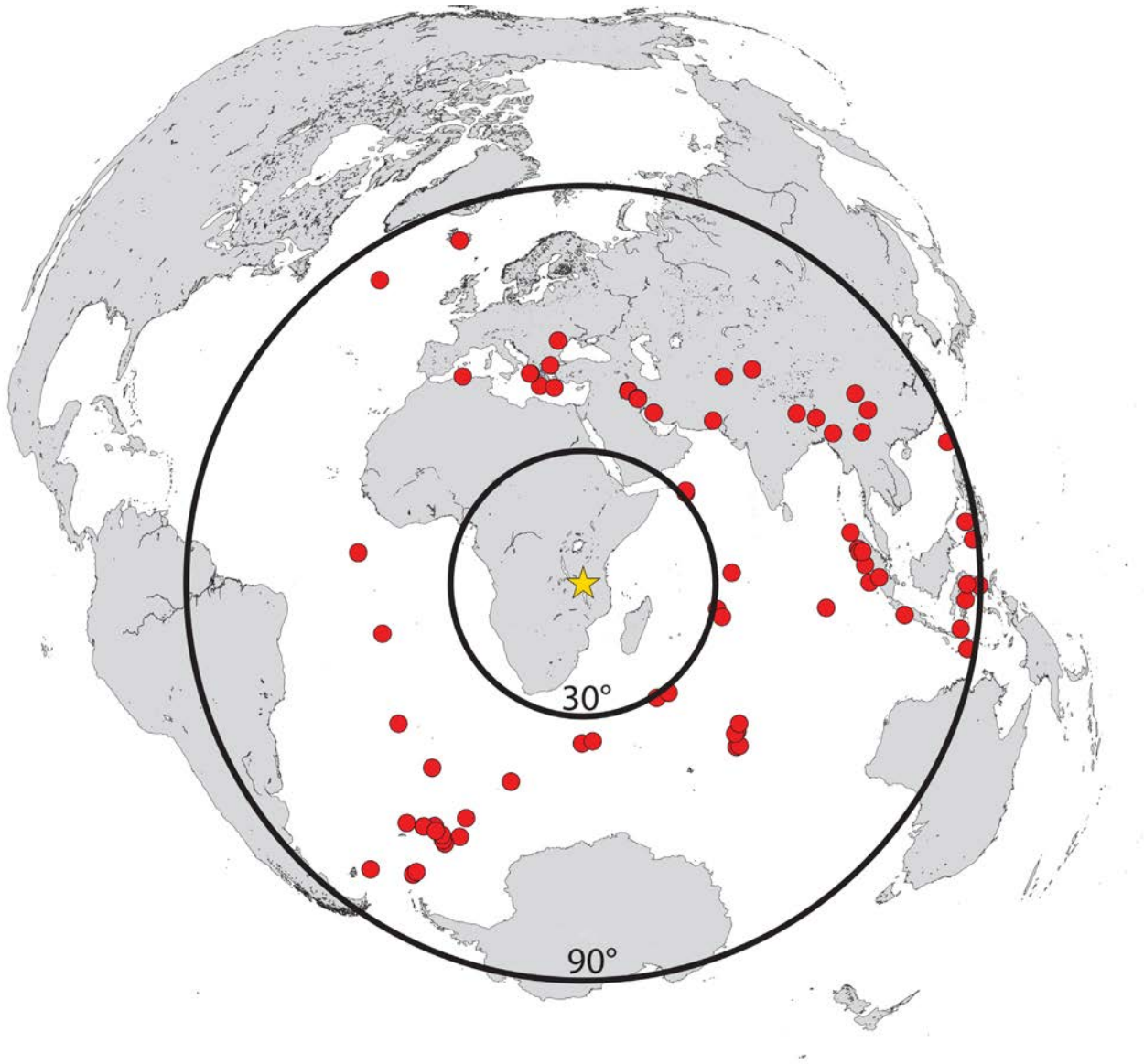


Figure 2. Map showing the distribution of earthquakes (red circles) used in this study. The star shows the centre of the network and the large circles show epicentral distances from the centre of the network.

functions and Rayleigh wave dispersion measurements (Table 1), and have used those estimates to comment on crustal thickness and composition, similar to the approach taken in this study. Using Poisson's ratio as a proxy for bulk crustal composition, an average Poisson's ratio of 0.24 ($Vp/Vs = 1.72$) indicates a felsic composition, while ratios of 0.26–0.27 ($Vp/Vs = 1.76$–1.79) indicate a felsic to intermediate composition and ratios of 0.28–0.30 ($Vp/Vs = 1.80$–1.88) indicate a mafic composition (Tarkov & Vavakin 1982; Christensen 1996). Average crustal shear wave velocities of 3.7 km s^{-1} or less suggest relatively felsic to intermediate composition crust, while average crustal shear wave velocities of 3.8 km s^{-1} or higher suggest relatively mafic composition (Christensen & Mooney 1995; Rudnick & Fountain 1995; Christensen 1996; Rudnick & Gao 2003). In the lower crust, velocities $\sim>3.9$ km s^{-1} indicate a mafic composition (Christensen & Mooney 1995; Rudnick & Fountain 1995; Christensen 1996; Rudnick & Gao 2003).

For the Mozambique Belt, Last *et al.* (1997) reported Moho depths of 36–39 km and Poisson's ratios of 0.24–0.27, and for the Ubendian Belt, Moho depths of 40–45 km and Poisson's ratio of 0.24–0.25. Julià *et al.* (2005) published similar results to Last *et al.* (1997) using the same dataset. For the Ubendian Belt, Tugume *et al.* (2012) obtained Moho depths of 35 to 49 km and Poisson's ratios of 0.24–0.28. Kim *et al.* (2009) obtained a Moho depth of 34 km and a Poisson's ratio of 0.27 for station PAND located in the Ubendian Belt, which is the same location as station MBEY in this study. For the Usagaran Belt, Tugume *et al.* (2012) reported Moho depths between 32 and 40 km and Poisson's ratios of 0.24–0.28, and for the Mozambique Belt, Moho depths of 37–42 km and Poisson's ratio of 0.24–0.27. For the Irumide Belt, Kachingwe *et al.* (2015) obtained Moho depths of 38–48 km and Poisson's ratios of 0.20–0.27. To the northwest of the study area in the rifted portions of the Ubendian Belt within the Rukwa and southern Tanganyika rifts, Hodgson *et al.* (2017) find a crustal thickness range of 31–42 km and

Downloaded from https://academic.oup.com/gji/article-abstract/215/2/1410/5068696 by Penn State University (Paterno Lib) user on 17 September 2018

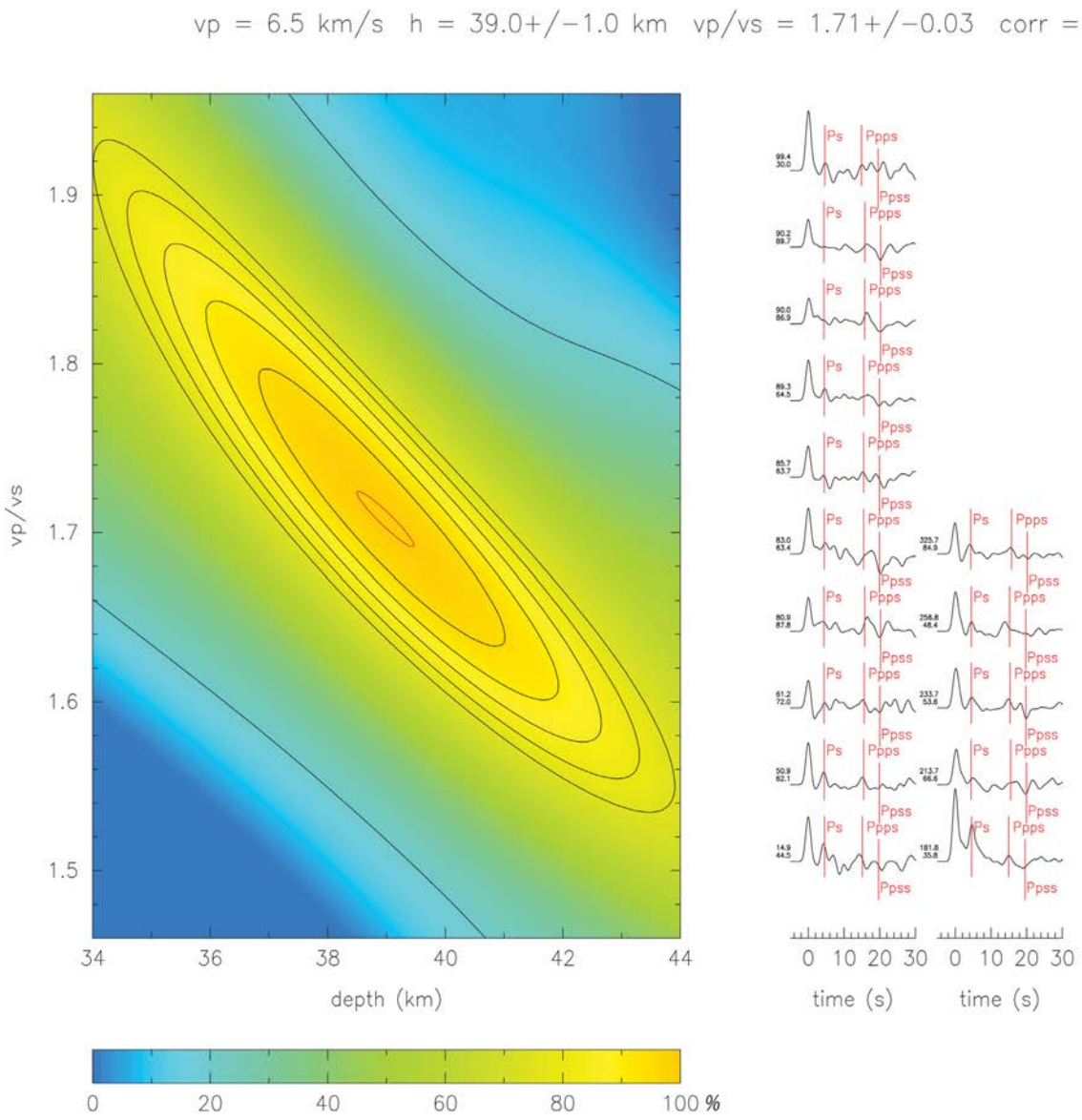


Figure 3. *H–k* stack result for station ZINI. Right-hand panel: receiver functions labelled by the event backazimuth (top number) and epicentral distance in degrees (bottom number). Left-hand panel: *H–k* parameter space with black contours, incremented by 10 per cent, mapping out the percentage values of the objective function in eq. (1). Red contour shows the 95 per cent confidence bound obtained using a bootstrapping method. The optimal values for H and *k* obtained are summarized along the top with formal uncertainties from the bootstrapping.

Poisson's ratios of 0.24–0.31. They infer some localized magmatic modification from the areas of thinner crust and higher Poisson's ratios, and lower crustal earthquakes.

4 DATA AND RECEIVER FUNCTIONS

The data used for this study were recorded between August 2013 and October 2015 by the SEGMeNT project broad-band seismic network (Shillington *et al.* 2016). The network consisted of 57 broad-band seismometers deployed across a 320 km × 340 km region around northern Lake Malawi (https://doi.org/10.7914/SN/YQ_2013; Fig. 1). Each station was equipped with a broad-band seismometer (Guralp CMG3T, Streckeisen STS-2 or Nanometrics 120 sec Trillium), a Reftek or Quanterra datalogger and a GPS (Global Positioning System) clock. During the first phase of deployment in August 2013, 14 stations were installed in and around the RVP (Fig. 1), and during the second phase in August 2014, 43 additional stations were deployed, including 17 in Malawi and 26 in Tanzania. All stations recorded data continuously through late October 2015. Additional station information is provided in the Supporting Information (Supplement A).

The teleseismic events used have magnitudes greater than 5.5 with epicentral distances between 30° and 90° from the recording stations and good signal-to-noise ratios, and represent about 10 per cent of all available $m > 5.5$ events in this distance range. Fig. 2 shows the overall event distribution, illustrating fairly good azimuthal coverage. A list of events used for computing receiver functions is provided in the Supporting Information (Supplement B).

P-wave receiver functions are time-series of *P*-to-*S* converted waves generated at seismic discontinuities (e.g. the Moho discontinuity) beneath a seismic station and contain multiple phases that

Downloaded from https://academic.oup.com/gji/article-abstract/215/2/1410/5068696 by Penn State University (Paterno Lib) user on 17 September 2018

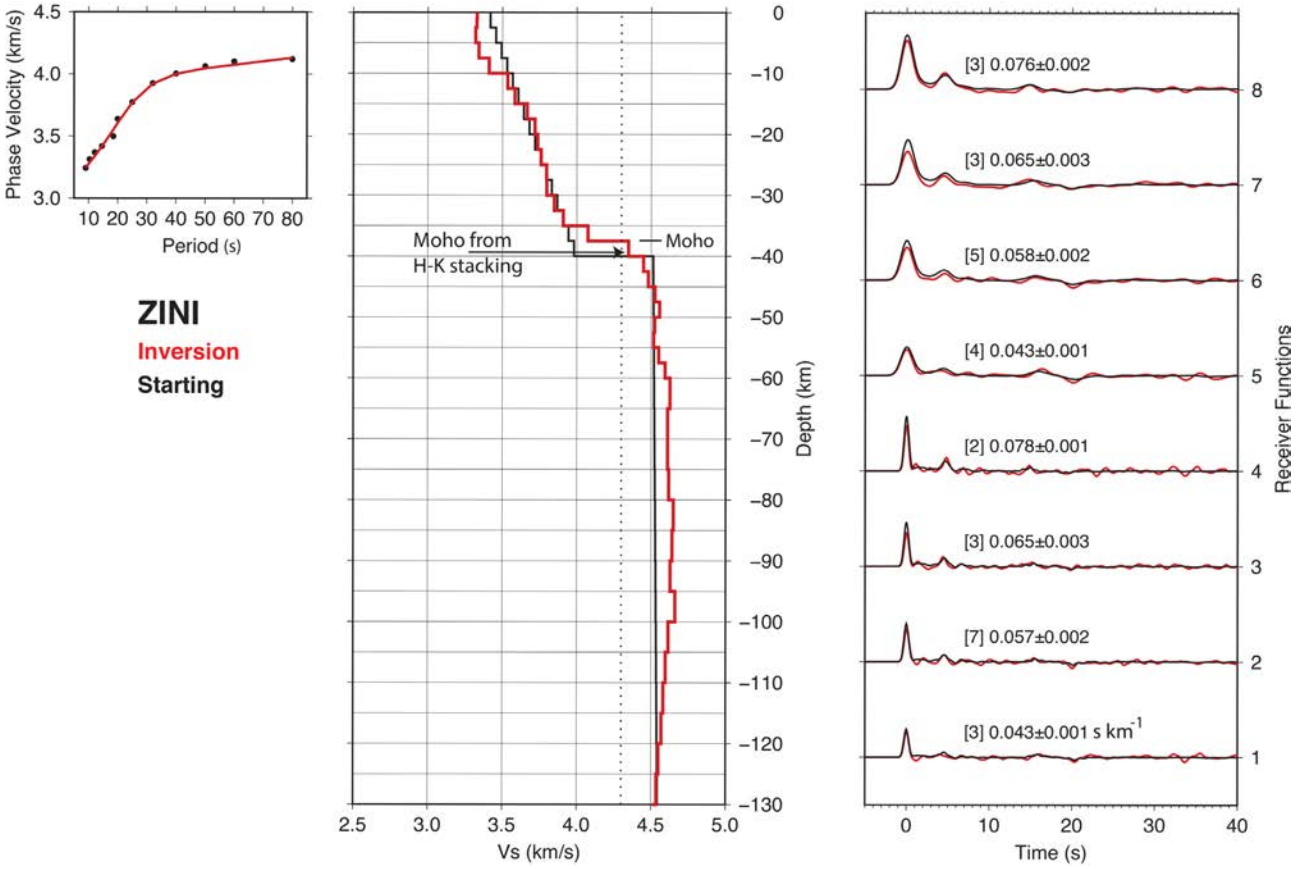


Figure 4. Results from the joint inversion for station ZINI. Left-hand panel: Rayleigh wave phase velocities. Centre panel: Shear wave velocity model. The dotted line at 4.3 km s^{-1} is shown for reference. Right-hand panel: receiver function stacks with low frequency (Gaussian 1.0) stacks on top and high frequency (Gaussian 2.5) stacks on bottom. Each group is ascending in ray parameter. Numbers in brackets show the number of receiver functions in each stack.

follow the main *P* arrival, including the Ps arrival from the Moho and its reverberations, PpPs and PpSS + PsPs (Langston 1979). Before computing *P*-wave receiver functions, each waveform was detrended, tapered, high pass filtered above 0.05 Hz to remove low frequency noise, and then low pass filtered below 8 Hz. The waveforms were cut to 10 s before and 110s after the first *P*-wave arrival, and the horizontal components were rotated into the great circle path to obtain the corresponding radial and transverse components. The vertical component was then deconvolved from the radial and transverse components using an iterative time-domain deconvolution with 500 iterations (Ligorria & Ammon 1999). For each event, receiver functions were computed for Gaussian bandwidths of 1.0 and 2.5, corresponding to frequency bands of $f \leq 0.5$ Hz and $f \leq 1.25$ Hz, respectively. The lower frequency receiver functions are better for observing long period phases from the lower crust and mantle, while the higher frequency receiver functions can reveal detailed phases from shallow crustal structure (Ligorria & Ammon 1999; Julià 2007).

The receiver functions were assessed for quality using a least-squares misfit in order to determine the per cent difference between the original radial component and the predicted radial component. This was done by convolving the original vertical component and the radial receiver function. Receiver functions with a fit of 85 per cent or better were used for modelling and interpretation, except for stations CHUN, KALO, KIFA, MFRI and THAN, where a fit of 75 per cent was used to obtain a sufficient number (≥4) of receiver functions for stacking.

5 METHODS

5.1 *H–k* stacking

The *H–k* stacking method was applied to the receiver functions to obtain estimates of crustal thickness (*H*) and *Vp*/*Vs* (*k*) (Zhu & Kanamori 2000). In this method, the receiver functions are transformed to the *H–k* parameter space by an objective function:

$$\mathrm{S}(\mathrm{H}, k) = \sum_{j=1}^{N} w_1 r_j(t_1) + w_2 r_j(t_2) - w_3 r_j(t_3), \quad (1)$$

where t_i are the traveltimes for the three converted phase arrivals, Ps and PpPs and PsPs + PpSs, respectively, r_j, is the *j*th receiver function amplitude, N is the number of receiver functions and w_i are weights assigned to each phase ($\sum^{w_i} = 1$). For a simple layer-over-half space model, S(H, k) is maximum when H and k obtain optimal values.

To apply the *H–k* stacking method, weights for the converted phases and an average crustal *Vp* must be selected. A *Vp* of 6.5 km s^{-1} was chosen because it is consistent with average crustal *P*-wave velocities determined from previous studies of Precambrian crust in eastern Africa (Fuchs *et al.* 1997; Julia *et al.* 2005; Tugume *et al.* 2012, and references therein). For consistency with Tugume *et al.* (2012) and Kachingwe *et al.* (2015), values of $w_1 = 0.4$, $w_2 = 0.3$, $w_3 = 0.3$ were employed, which places close to equal weights on all the phases. However, for stations ENUK, GAWA, KAPK, KIPE, MATA, MBAM, MBHS, MFRI, NGON and WENY, weights of $w_1 = 0.6$, $w_2 = 0.1$, $w_3 = 0.3$ were used because the PpPs phase

Downloaded from https://academic.oup.com/gji/article-abstract/215/2/1410/5068696 by Penn State University (Paterno Lib) user on 17 September 2018

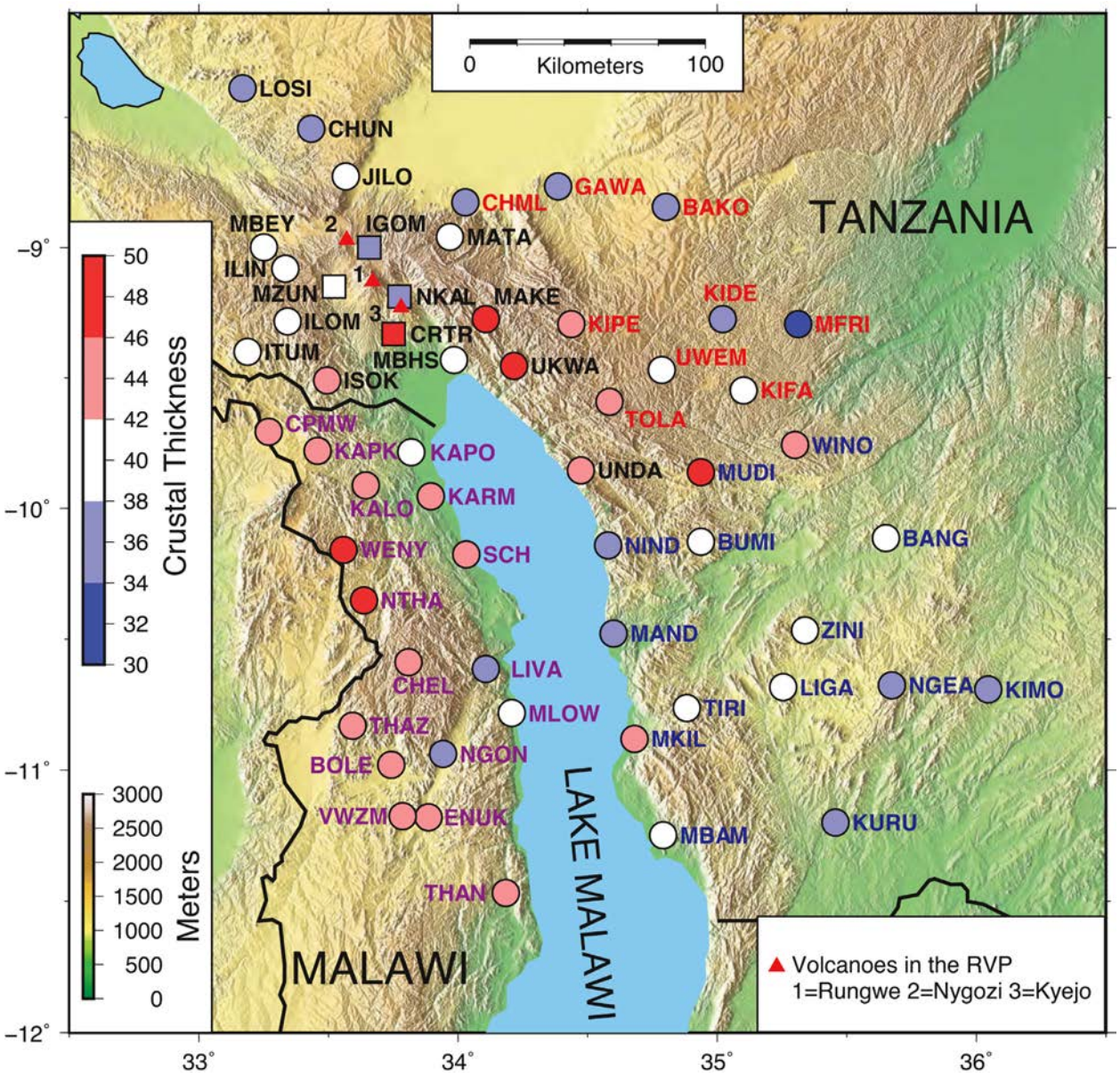


Figure 5. Topographic map showing Moho depth at each station from the H-*k* stacking results in Table 1. Moho depth for station NTHA is from the Moho Ps time only. Stations in the RVP are shown with squares. Stations with red text labels are in the Usgaran Belt, stations with blue text labels are in the Mozambique Belt, and stations with purple text labels are in the Irumide Belt.

was not as clearly visible in the receiver functions as the other two phases.

The *H*–*k* stacking method was performed using receiver functions generated with both 1.0 and 2.5 Gaussian filters for every station, except CHML and NTHA, as discussed below. Results using receiver functions computed with a Gaussian filter of 1.0 are reported for all but seven stations, where a Gaussian filter of 2.5 was used (Table 1). For those stations, the Moho converted phases were more clearly seen at higher frequencies than at lower frequencies. Receiver functions for station CHML were computed using a Gaussian filter of 0.5 because at this station the converted phases were more clearly visible at lower frequencies. For NTHA, the crustal reverberations (PpPs and PsPs + PpSs) could not be clearly seen on either low or high frequency receiver functions, and so *H* was estimated using the Ps time, an average crustal *Vp* of 6.5 km s^{-1}, a *Vp*/*Vs* ratio of 1.75 and the equation for *H* from Zandt & Ammon (1995):

$$H = t / \left[\left(\frac{1}{Vs^2} - p^2 \right)^{1/2} - \left(\frac{1}{Vp^2} - p^2 \right)^{1/2} \right], \quad (2)$$

where *t* is the arrival time of the Ps conversion, *p* is the ray parameter, *Vs* is the *S*-wave velocity determined from the *Vp*/*Vs* ratio and *Vp* is the *P*-wave velocity.

Formal uncertainties for *H* and *k* were obtained using a bootstrapping method, which involves repeating the stacking procedure 200 times with random, resampled data from the original dataset (Efron & Tibshirani 1991). These are minimal uncertainties as additional uncertainties in *H* and *k* arise because of the choice of the average crustal *Vp*. Thus, *H*–*k* stacks were also computed using a *Vp* of 6.3 and 6.8 km s^{-1} to estimate the uncertainties that arise from the choice of *Vp* used for the stacking. The combination of the

Downloaded from https://academic.oup.com/gji/article-abstract/215/2/1410/5068696 by Penn State University (Paterno Lib) user on 17 September 2018

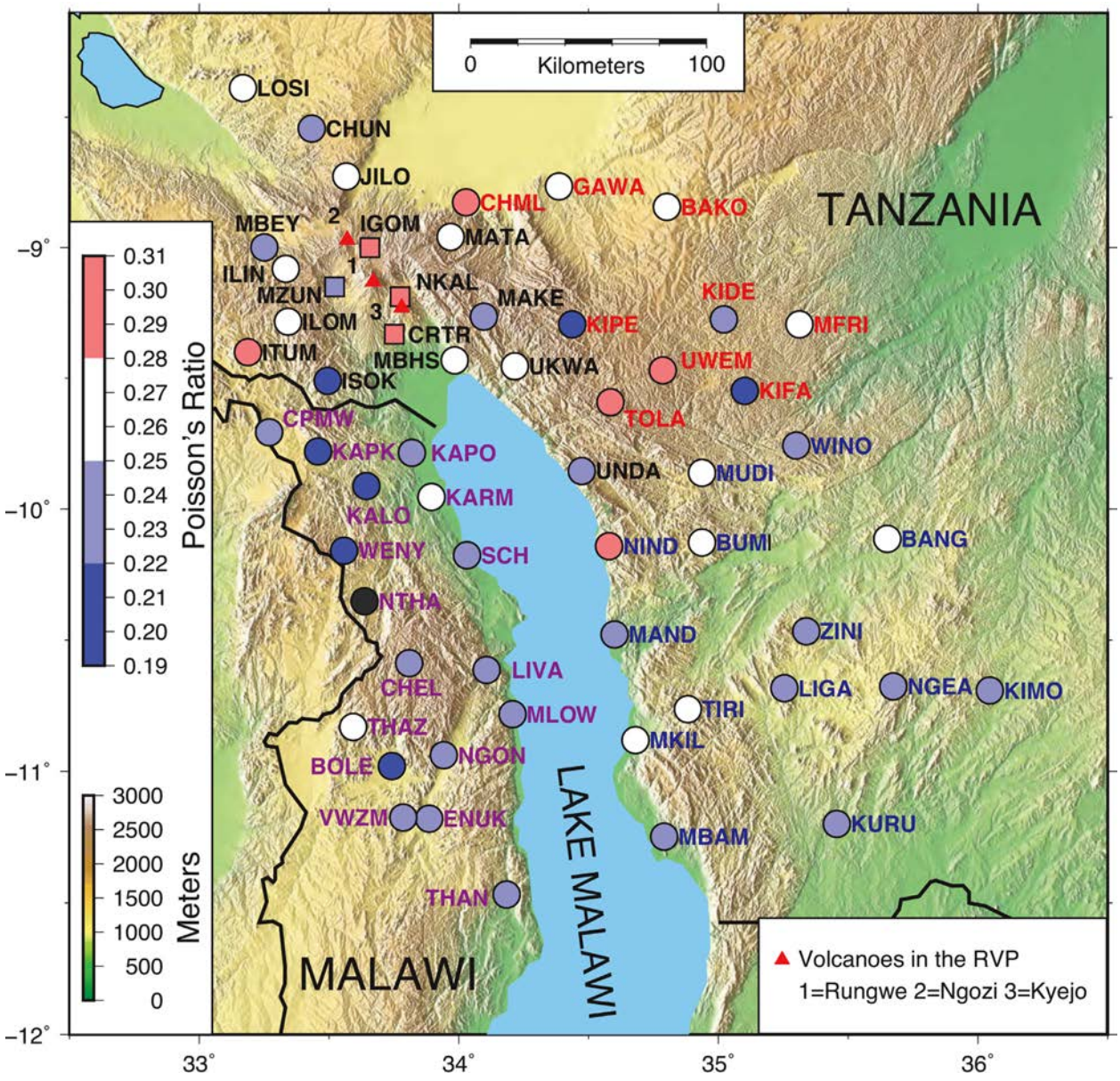


Figure 6. Topographic map showing Poisson's ratio at each station from the *H–k* stacking results in Table 1. No result was obtained for station NTHA. Stations in the RVP are shown with squares. Stations with red text labels are in the Usgaran Belt, stations with blue text labels are in the Mozambique Belt, and stations with purple text labels are in the Irumide Belt.

uncertainty estimates yields an overall uncertainty in Moho depth for each station of ∼3–4 km. Poisson's ratio changes by about 0.01 across the range of *Vp* used for the stacking (i.e. 6.3–6.8 km s^{-1}). Results for one station are illustrated in Fig. 3, and results for all of the other stations are provided in the Supporting Information (Supplement C).

5.2 Joint inversion

To obtain shear wave velocity models for each station, the receiver functions were jointly inverted with Rayleigh wave phase velocities between periods of 9 and 80 seconds from Accardo *et al.* (2017) using the method of Julià *et al.* (2000, 2003). The joint inversion method employs a linearized, least squares scheme to invert receiver functions and dispersion curves, and produces velocity models that are controlled by an *a priori* smoothing parameter. An *a priori* influence factor of 0.5 was used to control the influence of each data set, and a uniform smoothing parameter of 1.0 was used for all models.

Following Julia *et al.* (2000), the receiver function and surface wave dispersion datasets are equalized by the number of data points and physical units by dividing the RMS misfit for each data set by $N\sigma^2$, where 'N' is the number of data points and σ^2 is the variance. Since the receiver function data set may consist of several waveforms, the number of data points for the receiver function portion of the misfit function is the total number of points in the combined receiver function dataset. This makes the receiver function and surface wave dispersion datasets have equal weight in the misfit function, even when the number of receiver function waveforms is much larger than the number of dispersion curves.

Downloaded from https://academic.oup.com/gji/article-abstract/215/2/1410/5068696 by Penn State University (Paterno Lib) user on 17 September 2018

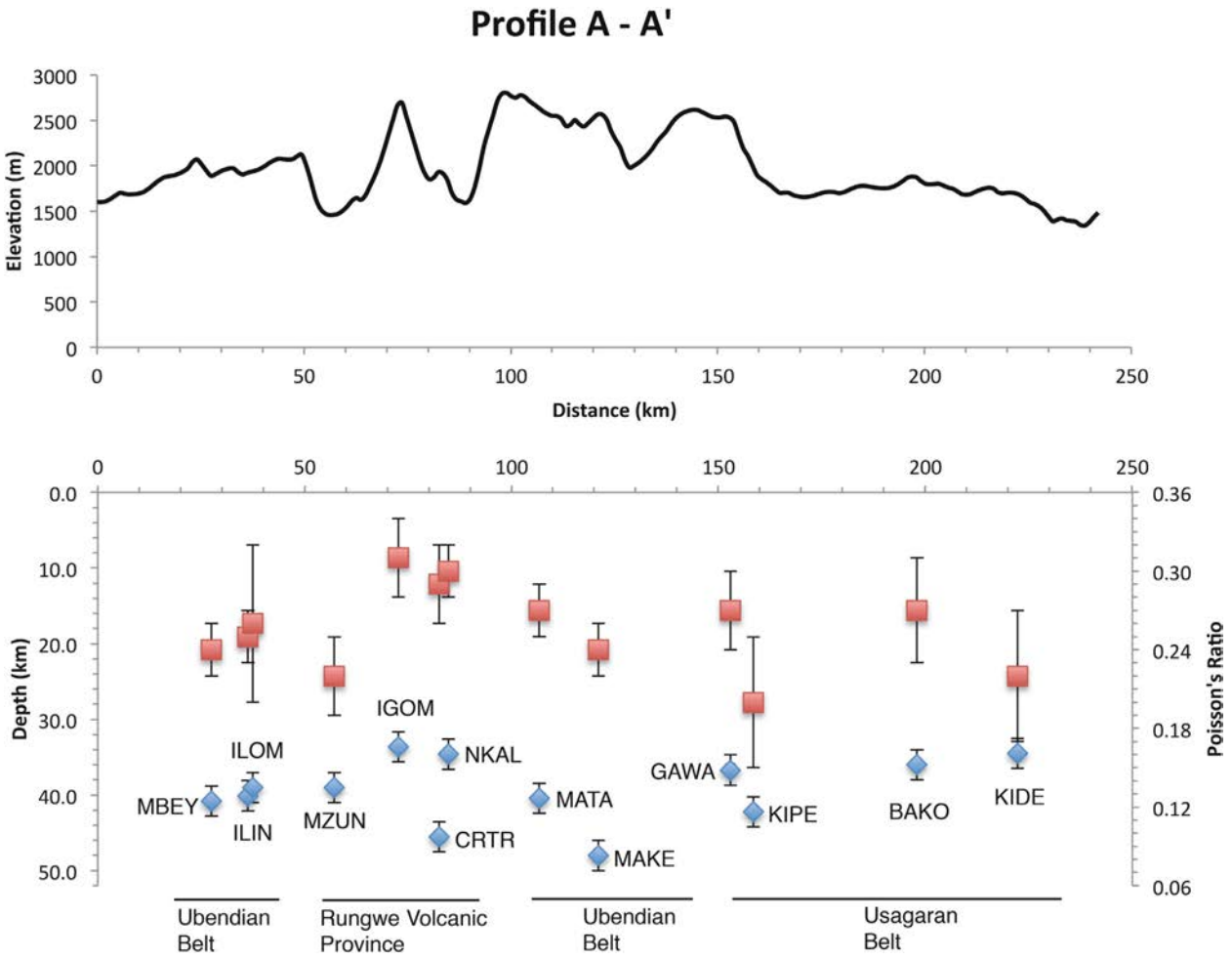


Figure 7. Moho depths (blue diamonds) and Poisson's ratios (red squares) along Profile A—A' across the RVP. The location of the profile is shown in Fig. 1.

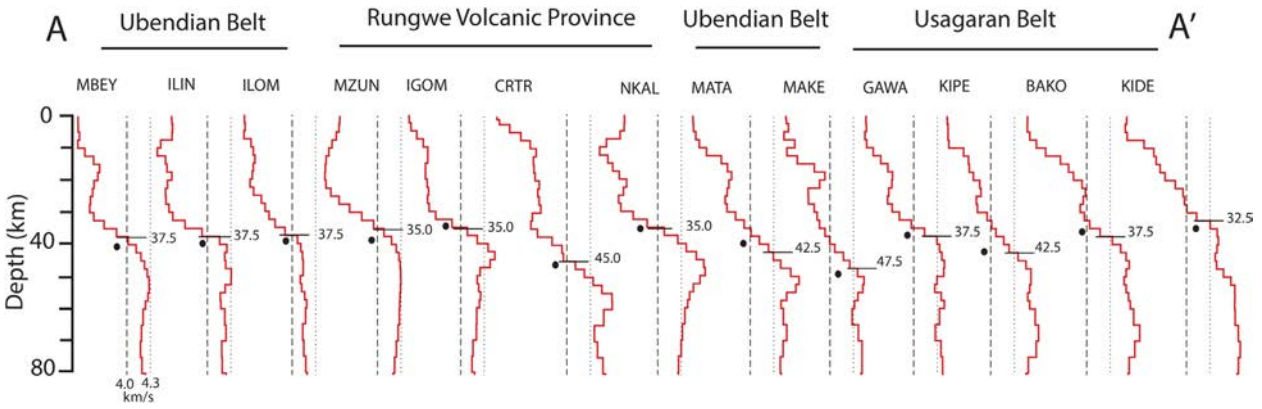


Figure 8. Shear wave velocity models for stations along Profile A–A' obtained from the joint inversion. Numbers next to horizontal black lines give Moho depths in kms from the joint inversion. Black dots show the Moho depth obtained from the *H–k* stacking. The dotted and dashed vertical lines at velocities of 4.0 and 4.3 km s^{-1} are shown for reference.

Prior to jointly inverting the receiver functions and phase velocities, the receiver functions were stacked using ray parameter bins of 0.04 to 0.049, 0.05 to 0.059, 0.06 to 0.069 and 0.07 to 0.079 s km^{-1}. For each station, receiver functions were stacked for two sets of overlapping frequency bands; that is low frequency of $f < 0.5$ Hz and high frequency of $f < 1.25$ Hz, corresponding to Gaussian filter widths of 1.0 and 2.5, respectively.

The starting model used for the inversion has a 40-km-thick crust and a linear shear wave velocity increase from 3.4 km s^{-1} at the surface to 4.3 km s^{-1} at the Moho. The crust overlies a mantle with Preliminary Reference Earth Model (PREM) velocities (Dziewonski & Anderson 1981). In the inversion, layer velocities were fixed to PREM values below 250 km, where the dispersion measurements have little, if any, sensitivity, and are not allowed to vary. The model parametrization consisted of layers of uniform

Downloaded from https://academic.oup.com/gji/article-abstract/215/2/1410/5068696 by Penn State University (Paterno Lib) user on 17 September 2018

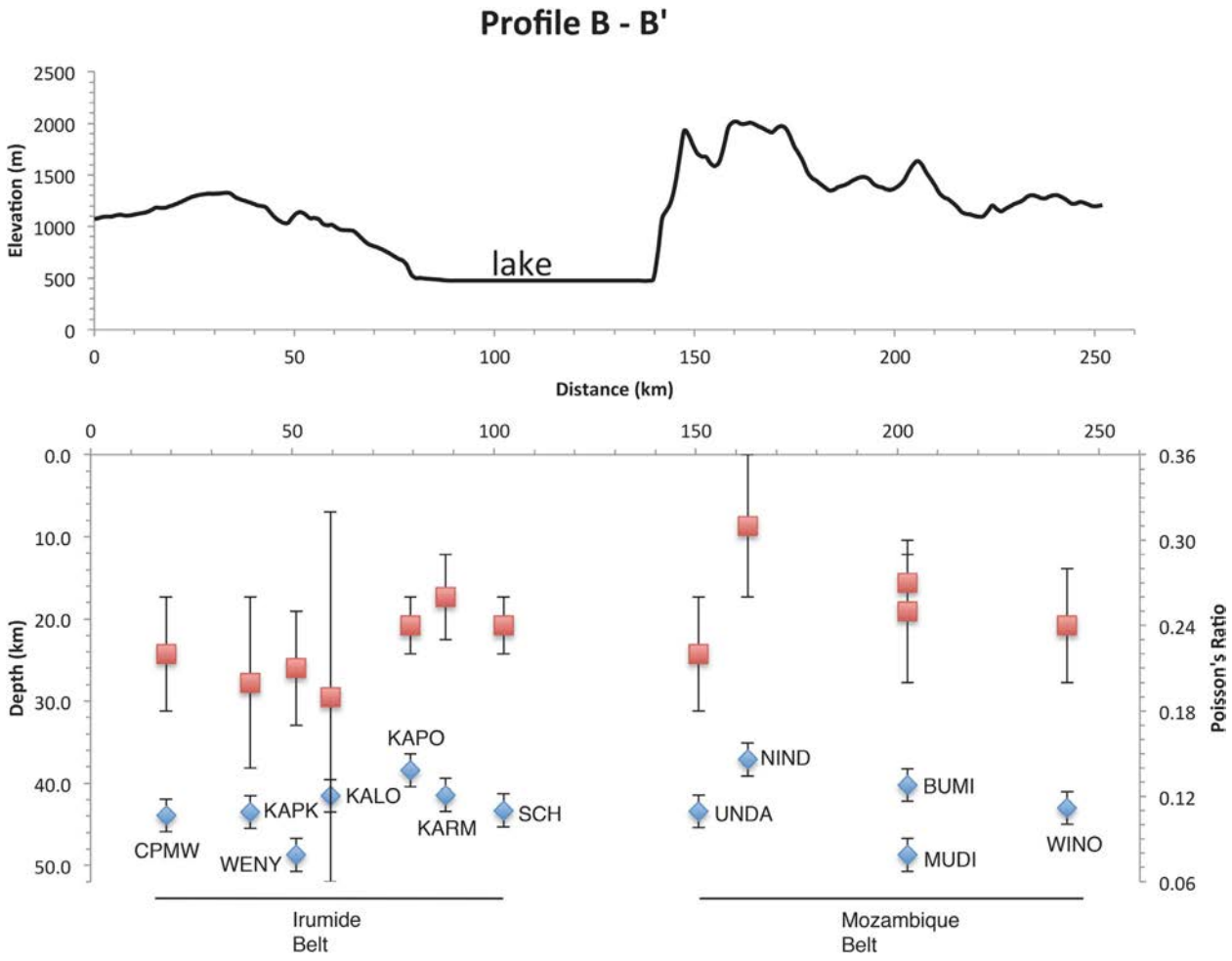


Figure 9. Moho depths (blue diamonds) and Poisson's ratios (red squares) along Profile B–B' across Lake Malawi. The location of the profile is shown in Fig. 1.

velocity that increase in thickness with depth. Layer thicknesses were 1–1.5 km at the top of the model, 2.5 km between 2.5 and 55 km depth, 5 km between 55 and 130 km depth, and 10 km below 130 km depth.

Uncertainties in the velocity models were estimated using the approach of Julià *et al.* (2005) by repeating inversions for a range of inversion parameters. The uncertainties in the shear wave velocities resulting from this process are ∼0.1 km s^{-1} for crustal layers and ∼0.2 km s^{-1} for the upper mantle layers, which leads to uncertainties in crustal thickness estimates of ±2.5 km. In addition to the model uncertainties, a qualitative assessment of the results, graded from A to D, was made based on the number and quality of the receiver function waveforms and how well the synthetics visually fit the data. Results with a grade of D were discarded. The velocity model and fits to the data from the inversion for one station are illustrated in Fig. 4, and similar figures for the other stations can be found in the supplemental material (file C).

6 RESULTS

Shear wave velocities for lower crustal lithologies tend not to exceed 4.3 km s^{-1} and velocities greater than 4.3 km s^{-1} are more common for mantle lithologies, provided that the mantle has not been thermally perturbed (Christensen & Mooney 1995; Christensen 1996). Therefore, following the approach by Tugume *et al.* (2012) and Kachingwe *et al.* (2015) for eastern Africa, in the joint inversion models the Moho is defined as the depth at which the shear wave velocity is equal to or exceeds 4.3 km s^{-1}. For most stations, there is a significant increase in velocity (i.e. velocity discontinuity) at the depth where the velocity exceeds 4.3 km s^{-1}, except for 16 stations. For stations CPMW, ISOK, KALO, KAPK, LOSI and UWEM, which are not within or close to the RVP, the shear wave velocity increase is gradational from the lower crust to the upper mantle, and the Moho is placed at the depth where the *Vs* equals or exceeds 4.3 km s^{-1}. For stations CHUN, CRTR, IGOM, ILIN, ILOM, ITUM, JILO, MBEY, MZUN and NKAL, which are within or near to the RVP where the mantle has been thermally perturbed (Adams *et al.* 2012; O'Donnell *et al.* 2013; Accardo *et al.* 2017), there is a discontinuity in velocity at a shallower depth, typically where the velocity increases from around 3.8 to 4.1 or 4.2 km s^{-1}. For these stations, the Moho is placed at the depth of the velocity increase. Stable inversion results were not obtained for stations CHML and WENY.

Results from the *H–k* stacking and joint inversion are summarized in Table 1 and illustrated in Figs 5 and 6. There is good agreement in the results from the two methods, within the reported uncertainties. The Poisson's ratios (Table 1, Fig. 6) were calculated using the *Vp*/*Vs* ratios obtained from the *H–k* stacking.

Downloaded from https://academic.oup.com/gji/article-abstract/215/2/1410/5068696 by Penn State University (Paterno Lib) user on 17 September 2018

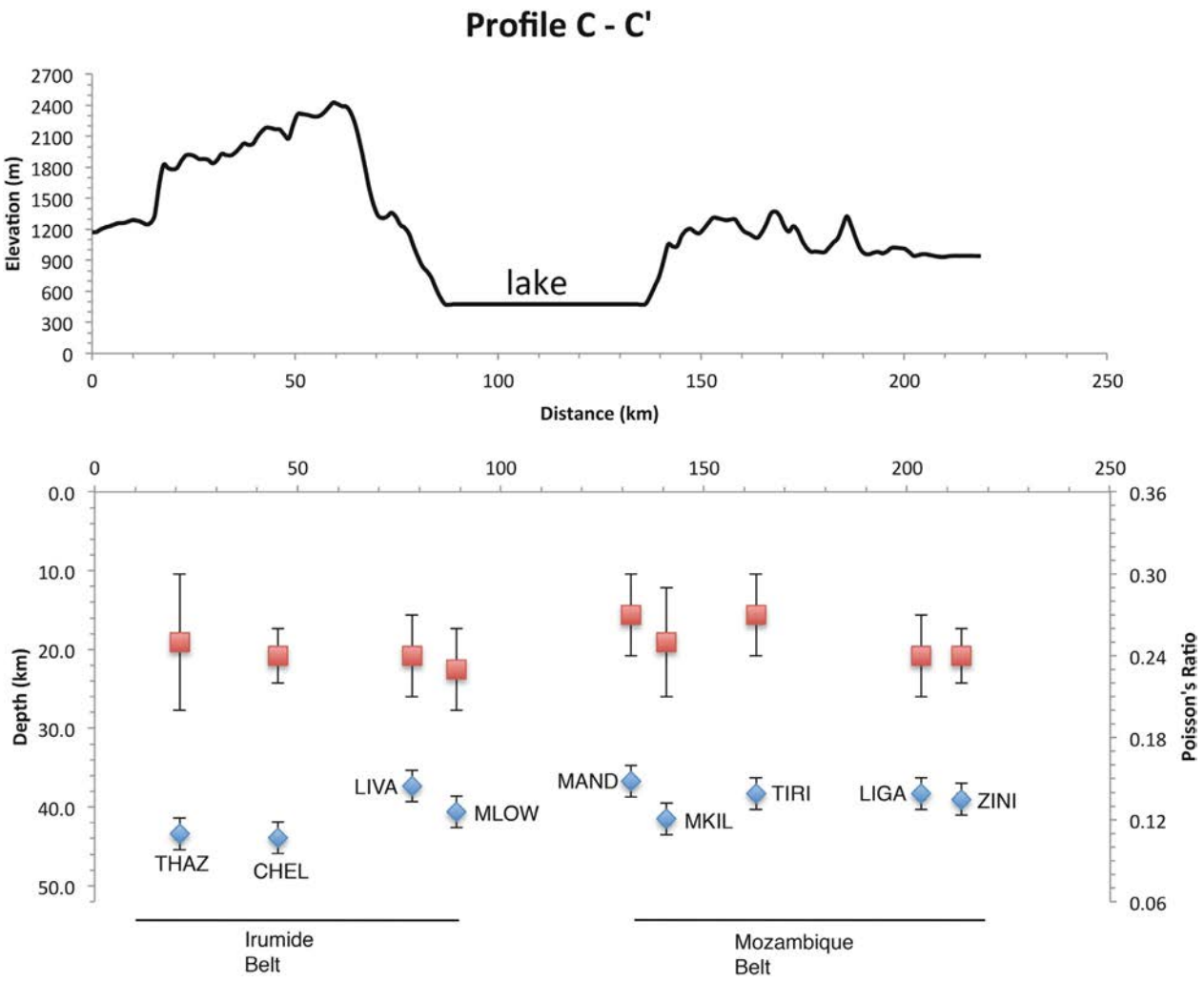


Figure 10. Moho depths (blue diamonds) and Poisson's ratios (red squares) along Profile C–C' across Lake Malawi. The location of the profile is shown in Fig. 1.

For the Ubendian Belt stations, crustal thickness varies from 37 to 49 km, with an average of 41 ± 4 km (*SD*). Poisson's ratio ranges from 0.19 to 0.28, with an average of 0.25 ± 0.02. The average crustal shear wave velocity is 3.6 ± 0.1 km s^{-1}. For stations in the Usagaran Belt, the average crustal thickness varies from 31 to 44 km, with an average of 38 ± 3 km. Poisson's ratio ranges from 0.20 to 0.30, with an average of 0.26 ± 0.04. The average crustal shear wave velocity is 3.7 ± 0.1 km s^{-1}. For the Irumide Belt stations, crustal thickness varies from 37 to 49 km, with an average of 42 ± 3 km. Poisson's ratio ranges from 0.19 to 0.26, with an average of 0.23 ± 0.02. The average crustal shear wave velocity is 3.6 ± 0.1 km s^{-1}. In the Mozambique Belt, crustal thickness varies from 37 to 49 km, with an average of 40 ± 3 km. Poisson's ratio ranges from 0.22 to 0.31, with an average of 0.25 ± 0.02. The average crustal shear wave velocity is 3.7 ± 0.1 km s^{-1}. For stations located in the Rungwe Volcanic Province, crustal thickness varies from 34 to 46 km, with an average of 39 ± 5 km. Poisson's ratio ranges from 0.22 to 0.31, with an average of 0.28 ± 0.04. The average crustal shear wave velocity is 3.6 ± 0.05 km s^{-1}.

Stations along the flank of the Malawi rift within the Irumide, Ubendian and Mozambique belts show little evidence of crustal thinning with respect to the average crustal thickness of the respective mobile belts (Fig. 5). There is also little evidence for a dipping Moho beneath these stations as would be reflected in azimuthal variations in the receiver functions. Poisson's ratios at these stations are also not significantly different from the average for the respective mobile belts, expect for station NIND, which has an elevated Poisson's ratio of 0.31 (Fig. 6).

7 DISCUSSION

Results from previous studies are included in Table 1 for comparison to the results obtained in this study. The results from this study are consistent with previous studies and suggest few, if any, significant differences between the mean crustal thickness and composition of the Proterozoic terranes. For example, Tugume *et al.* (2012) obtained an average Moho depth of 42 km and Poisson's ratio of 0.26 for the Ubendian Belt, which are identical to the average Moho depth and Poisson's ratio obtained in this study. Conversely, to the northwest of the study area within the Ubendian Belt, crustal thickness estimates of 32–42 km are found, with Poisson's ratio ranging from 0.24 to 0.31 (Hodgson *et al.* 2017). Their thinnest crust (32–34 km) is found at the edge of a fault-bounded rift basin. Kachingwe *et al.* (2015) reported an average crustal thickness for the Irumide Belt of 43 km and a Poisson's ratio of 0.23, also identical to the results in this study. In previous studies of the Mozambique Belt,

Downloaded from https://academic.oup.com/gji/article-abstract/215/2/1410/5068696 by Penn State University (Paterno Lib) user on 17 September 2018

Tugume *et al.* (2012) and Kachingwe *et al.* (2015) reported Moho depths of 37–38 km and Poisson's ratio of 0.25–0.26. Similar results have been obtained in this study, with an average crustal thickness of 39 km and Poisson's ratio of 0.25.

The average Poisson's ratios for the Proterozoic mobile belt crust range from 0.23 to 0.26 and the average crustal shear wave velocity ranges from 3.6 to 3.7 km s^{-1} (Table 1). Both ranges are indicative of a bulk felsic to intermediate composition crust. The lowest shear wave velocities and Poisson's ratios are associated with the Irumide Belt. There is a large range in the thickness of mafic lower crust found within the mobile belts (i.e. layers at the bottom of the crust with shear wave velocities equal to or greater than 4.0 km s^{-1}). For many of the stations, there is only a few to about 10 km of the lower crust where velocities are high enough to indicate mafic compositions. However, at eight stations the thickness of the mafic lower crust is $\geq$10 km (Table 1). These stations are spread throughout the Ubendian, Usagaran, Irumide and Mozambique belts, and are not clustered in any one area. The origin of the thick mafic lower crust is uncertain.

If the RVP crust has been modified by Cenozoic magmatism, modifications to the crust could manifest as thickened crust from magmatic addition, high average crustal shear wave velocities because of mafic intrusions, low velocities in the crust resulting from the presence of partial melt, or high Poisson's ratios either from mafic material in the crust, elevated temperatures or the presence of partial melt. To help determine whether or not the RVP crust has been modified magmatically, results from several stations within and around the RVP are plotted in Figs 7 and 8. Fig. 7 shows Moho depths and Poisson's ratios projected onto profile A-A', and Fig. 8 shows the *Vs* models from the joint inversion. Stations in the RVP have crustal thicknesses ranging from 34 to 46 km and Poisson's ratios of 0.29–0.31, with the exception of MZUN, which has a Poisson's ratio of 0.22. Stations located immediately around the RVP (MAKE, MATA, MBEY, ILIN and ILOM) show crustal thickness of 39 to 48 km and Poisson's ratios of 0.24–0.27.

The similar crustal thicknesses beneath and surrounding the RVP indicate little, if any, crustal thickening from magmatic addition to the crust (Fig. 7), as is seen in the magma-rich Eastern rift area (e.g. Dugda *et al.* 2007; Plasman *et al.* 2017). In addition, the shear wave velocities in the middle and lower parts of the crust beneath the RVP stations are lower than what would be expected for a crust with significant mafic magmatic intrusions (Fig. 8). The crustal shear velocities for the RVP stations also look similar to the velocity profiles for the stations in the Ubendian belt. In contrast, the velocities in the middle and lower parts of the crust in the Usagaran belt are significantly higher. The thickness and velocity structure of the RVP crust therefore does not appear to be significantly different from the surrounding mobile belt crust.

The higher Poisson's ratios for three of the RVP stations, on the other hand, could indicate either a more mafic crust and/or the presence of partial melt in the crust. But, as noted above, the lower average shear wave velocities for the RVP crust of 3.6 km s^{-1} (Table 1) and the low shear wave velocities in the middle and lower crust are not consistent with a mafic crust. Therefore, it is more likely that the high Poisson's ratios suggest the presence of partial melt in the crust beneath the RVP than significant additions of mafic rock to the crust.

These results may have important implications for evaluating the influence of magmatism on the origin and evolution of the Malawi rift. Most significantly, although the ages of volcanic rocks from the RVP suggest that there has been long-lived magmatism here, the absence of pronounced changes in crustal composition or thickness suggest that it is volumetrically small. For example, if the RVP magmatism has not led to resolvable modifications in the thickness and velocity structure of the crust beneath the RVP, then it may be even more challenging to determine the extent to which the rifted crust away from the RVP has been modified magmatically.

Some studies of early stage rifts in the Eastern rift and Western rift reveal evidence for an outward-dipping Moho, a gradational Moho and high Poisson's ratio suggesting magmatic underplating and stretching localized to the fault bounded rift valley (Wölbern *et al.* 2010; Hodgson *et al.* 2017; Plasman *et al.* 2017). However, there is little evidence in our results for thinning of the crust under the rift shoulders and/or a gradational Moho, or high Poisson's ratios (Figs 9 and 10). None of the stations along the edge of the rift have a gradational Moho, and only one station (NIND) has an elevated Poisson's ratio (Figs 9 and 10). Thus, the northern Malawi rift may be different in these respects to other early stage rifts in eastern Africa.

Our results, combined with results of gravity and topography models that assume steep, deep border faults in relatively strong lithosphere (Ebinger *et al.* 1991; Ellis & King 1991), also indicate that crustal thinning in the northern Malawi rift must be highly focused beneath the centres of rift basin segments. Furthermore, the absence of thinned crust beneath the uplifted rift flanks requires the border faults to be steep and for lower crustal strain to be localized. A breakaway or detachment fault in the mid to lower crust is not consistent with our findings.

8 SUMMARY AND CONCLUSIONS

In summary, estimates of crustal structure beneath 57 seismic stations in the SEGMeNT network have been obtained using the *H–k* stacking method and jointly inverting *P*-wave receiver functions with Rayleigh wave phase velocities. The average crustal thickness of the four stations in the RVP is 39 $\pm$ 5 km, the average Poisson's ratio is 0.28 $\pm$ 0.04 ($Vp/Vs = 1.83$), and the average crustal shear wave velocity is 3.6 km s^{-1}. The average crustal thickness for stations in the Proterozoic terranes ranges between 38 and 42 km. In most of the terranes, the average Poisson's ratios are between 0.25 and 0.26 ($Vp/Vs = 1.73$–1.76), with the exception of the Irumide Belt, which has a Poisson's ratio of 0.23 $\pm$ 0.02 ($Vp/Vs = 1.68$). The average crustal shear wave velocities for all Proterozoic terranes are between 3.6 and 3.7 km s^{-1}. There are no discernable differences in reported crustal thicknesses and Poisson's ratios for the Precambrian terranes compared to results reported in previous studies.

Within the RVP, the high crustal Poisson's ratio and the low average crustal *Vs* can be attributed to elevated temperatures and partial melting associated with the RVP magmatism. There is little evidence for significant additions of mafic rock to the crust. There is also no evidence that the Cenozoic magmatism of the RVP has modified crustal structure around the northern margin of the Malawi rift.

With regard to the formation of the Malawi rift, there is little indication for any crustal thinning beneath the rift flanks on either side of the rift, or a gradational Moho or elevated Poisson's ratio, as have been found beneath the flanks of some other early stage rifts in eastern Africa. Consequently, crustal thinning in the northern Malawi rift must be highly focused beneath the centres of rift basin segments, consistent with predictions of steep, deep border fault models.

Downloaded from https://academic.oup.com/gji/article-abstract/215/2/1410/5068696 by Penn State University (Paterno Lib) user on 17 September 2018

ACKNOWLEDGEMENTS

Funding for this program was provided by the National Science Foundation (NSF) through Awards EAR-1109293, 1109302, 1109512, 1110882 and 1110921, and by Lamont-Doherty Earth Observatory of Columbia University. Acquisition of this dataset would not have been possible without the support from communities in the study area, national and regional governmental entities in Malawi and Tanzania, and the IRIS PASSCAL program. We thank two anonymous reviewers for helpful comments that substantially improved this paper.

REFERENCES

Accardo, N. *et al.*, 2017. Surface-wave imaging of the weakly-extended Malawi Rift from ambient-noise and teleseismic Rayleigh waves from onshore and lake-bottom seismometers, *Geophys. J. Int.,* **209,** 1892–1905.

Accardo, N.J. *et al.*, The growth and interaction of large border faults in the Malawi Rift revealed by 3D seismic refraction imaging, *J. geophys. Res.,* in review.

Adams, A., Nyblade, A. & Weeraratne, D., 2012. Upper mantle shear wave velocity structure beneath the east African plateau: evidence for a deep, plateauwide low velocity anomaly, *Geophys. J. Int.,* **189,** 123–142.

Begg, G., Griffin, W., Natapov, L., O'Reilly, S., Grand, S., O'Neill, C. & Bowden, P., 2009. The lithospheric architecture of Africa: seismic tomography, mantle petrology, and tectonic evolution, *Geosphere,* 23–50.

Brune, S., Williams, S.E., Butterworth, N.P. & Muller, D., 2016. Abrupt plate accelerations shape rifted continental margins, *Nature,* **536**(7615), 201–204.

Buck, W., 2004. Consequences of asthenospheric variability on continental rifting, in *Rheology and Deformation of the Lithosphere at Comntinental Margins,* pp. 1–31, eds Karner, G.D., Taylor, B., Driscolland, N.W. & Kohlstedt, D.L., Columbia University Press.

Burov, E. & Poliakov, A., 2001. Erosion and rheology controls on synrift and postrift evolution: verifying old and new ideas using a fully coupled numerical model, *J. geophys. Res.: Solid Earth,* **106,** 16461–16481.

Cahen, L. & Snelling, N., 1983. *The Geochronology and Evolution of Africa,* Clarendon Press.

Casey, M., Ebinger, C., Keir, D., Gloaguen, R. & Mohamed, F., 2006. Extension by dyke extension and faulting in an incipient oceanic rift: Ethiopian rift, Africa, in *The Afar Volcanic Province within the East African Rift System,* Vol. **259,** pp. 143–164, eds Yirgu, G., Ebinger, C. & Maguire, P., Geol. Soc. London Spec. Pub.

Christensen, N., 1996. Possion's ratio and crustal seismology, *J. geophys. Res.,* **101,** 3139–3156.

Christensen, N. & Mooney, W., 1995. Seismic velocity structure and composition of the continental-crust—a global view, *J. geophys. Res.: Solid Earth,* **100,** 9761–9788.

Cox, K., 1970. Tectonics and volcanism of the Karoo period and their bearing on the postulated fragmentation of Gondwanaland, in *African Magmatism and Tectonics,* pp. 211–235, Oliver and Boyd.

De Waele, B., Kampunzu, A.B., Mapani, B. & Tembo, F., 2006. The Mesoproterozoic irumide belt of Zambia, *J. Afr. Earth Sci.,* **46,** 36–70.

De Waele, B., Johnson, S. & Pisarevsky, S., 2008. Palaeoproterozoic to Neoproterozoic growth and evolution of the eastern Congo Craton: its role in the Rodinia puzzle, *Precambrian Res.,* **160,** 127–141.

Dugda, M.T., Nyblade, A.A. & Julia, J., 2007. Thin lithosphere beneath the Ethiopian Plateau revealed by a joint inversion of Rayleigh wave group velocities and receiver functions, *J. geophys. Res.,* **112,** B08305.

Dziewonski, A. & Anderson, D., 1981. Preliminary reference earth model, *Phys. Earth planet. Inter.,* **25,** 297–356.

Ebinger, C., Deino, A., Drake, R. & Tesha, A., 1989. Chronology of volcanism and rift basin propagation—Rungwe volcanic province, east Africa, *J. geophys. Res.: Solid Earth,* **94,** 15 785–15 803.

Ebinger, C., Karner, G. & Weissel, J., 1991. Mechanical strength of extended continental lithosphere: examples from the Western rift, East Africa, *Tectonics,* **10,** 1239–1256.

Efron, B. & Tibshirani, R., 1991. Statistical data analysis in computer age, *Science,* **253,** 390–395.

Ellis, M. & King, G, 1991. Structural control of flank volcanism in continental rifts, *Science,* **254,** 839–842.

Fontijn, K., Delvaux, D., Ernst, G., Kervyn, M., Mbede, E. & Jacobs, P., 2010a. Tectonic control over active volcanism at a range of scales: case of the Rungwe Volcanic Province, SW Tanzania; and hazard implications, *J. Afr. Earth Sci.,* **58,** 764–777.

Fontijn, K., Ernst, G., Elburg, M., Williamson, D., Abdallah, E., Kwelwa, S. & Jacobs, P., 2010b. Holocene explosive eruptions in the rungwe volcanic province, Tanzania, *J. Volc. Geotherm. Res.,* **196,** 91–110.

Fontijn, K., Williamson, D., Mbede, E. & Ernst, G., 2012. The rungwe volcanic province, Tanzania—a volcanological review, *J. Afr. Earth Sci.,* **63,** 12–31.

Fritz, H. *et al.*, 2013. Orogen styles in the East African Orogen: a review of the Neoproterozoic to Cambrian tectonic evolution, *J. Afr. Earth Sci.,* **86,** 65–106

Fuchs, K., Altherr, B., Muller, B. & Prodehl, C. eds., 1997. Structure and dynamic processes in the lithosphere of the Afro-Arabian rift system, *Tectonophysics,* **278**(special issue), 1–352.

Furman, T., 2007. Geochemistry of East African Rift basalts: an overview, *J. Afr. Earth Sci.,* **48,** 147–160.

Gummert, M., Lindenfeld, M., Wölbern, I., Rümpker, G., Celestin, K. & Batte, A., 2015. Crustal structure and high-resolution Moho topography across the Rwenzori region (Albertine rift) from P-receiver functions, *Geol. Soc., Lond. Spec. Publ.,* **420,** 69–82.

Hodgson, I., Illsley-Kemp, F., Gallacher, R.J., Keir, D., Ebinger, C.J. & Mtelela, K., 2017. Crustal structure at a young continental rift: a receiver function study from the Tanganyika Rift, *Tectonics,* **36**.

Huismans, R. & Beaumont, C., 2011. Depth-dependent extension, two-stage breakup and cratonic underplating at rifted margins, *Nature,* **473,** 74.

Jakovlev, A., Rumpker, G., Schmeling, H., Koulakov, I., Lindenfeld, M. & Wallner, H., 2013. Seismic images of magmatic rifting beneath the western branch of the East African rift, *Geochem. Geophys. Geosyst.,* **14**.

Julià, J., Ammon, C., Herrmann, R. & Correig, A., 2000. Joint inversion of receiver function and surface wave dispersion observations, *Geophys. J. Int.,* **143,** 99–112.

Julià, J., Ammon, C. & Herrmann, R., 2003. Lithospheric structure of the Arabian shield from the joint inversion of receiver functions and surface-wave group velocities, *Tectonophysics,* **371,** 1–21.

Julià, J., Ammon, C. & Nyblade, A., 2005. Evidence for mafic lower crust in Tanzania, east Africa, from joint inversion of receiver functions and Rayleigh wave dispersion velocities, *Geophys. J. Int.,* **162,** 555–569.

Julia, J., 2007. Constraining velocity and density contrasts across the crust-mantle boundary with receiver function amplitudes, *Geophys. J. Int.,* **171,** 286–301.

Kachingwe, M., Nyblade, A. & Julia, J., 2015. Crustal structure of Precambrian terranes in the southern African subcontinent with implications for secular variation in crustal genesis, *Geophys. J. Int.,* **202,** 533–547.

Kim, S., Nyblade, A. & Baag, C., 2009. Crustal velocity structure of the Rukwa rift in the western branch of the east African rift system, *S. Afr. J. Geol.,* **112,** 251–260.

Langston, C., 1979. Structure under Mount Rainier, Washington, inferred from teleseismic body waves, *J. geophys. Res.,* **84,** 4749–4762.

Last, R., Nyblade, A., Langston, C. & Owens, T., 1997. Crustal structure of the east African plateau from receiver functions and Rayleigh wave phase velocities, *J. geophys. Res.: Solid Earth,* **102,** 24469–24483.

Lenoir, J., Liégeois, J., Theunissen, K. & Klerkx, J., 1994. The Palaeoproterozoic Ubendian shear belt in Tanzania: geochronology and structure, *J. Afr. Earth Sci.,* **19,** 169–184.

Ligorria, J. & Ammon, C., 1999. Iterative deconvolution and receiver-function estimation, *Bull. seism. Soc. Am.,* **89,** 1395–1400.

McConnell, R.B., 1972. Geological development of the rift system of eastern Africa, *Bull. geol. Soc. Am.,* **83,** 2549–2572.

Mesko, G.T., Class, C., Maqway, M.D., Boniface, N., Manya, S. & Hemming, S.R., 2014. The timing of early Magmatism and extension in the Southern East African rift: Tracking geochemical source variability with 40Ar/39Ar

Downloaded from https://academic.oup.com/gji/article-abstract/215/2/1410/5068696 by Penn State University (Paterno Lib) user on 17 September 2018

geochronology at the Rungwe volcanic province, SW Tanzania, in *AGU Fall Meeting Abstracts,* V51A–4730.

Mulibo, G. & Nyblade, A., 2016. The seismotectonics of southeastern Tanzania: implications for the propagation of the Eastern Branch of the East African Rift, *Tectonophysics,* **674,** 20–30.

O'Donnell, J.P., Adams, A., Nyblade, A., Mulibo, G. & Tugume, F., 2013. The uppermost mantle shear wave velocity structure of eastern Africa from Rayleigh wave tomography: constraints on rift evolution, *Geophys. J. Int.,* **194,** 961–978.

Olive, J-A., Behn, M., Mittelstaedt, E., Ito, G. & Klein, B., 2016. The role of elasticity in simulating long-term tectonic extension, *Geophys. J. Int.,* **205,** 728–743.

Plasman, M., Tiberi, C., Ebinger, C., Gautier, S., Albaric, J., Peyrat, S. & Gama, R., 2017. Lithospheric low-velocity zones associated with a magmatic segment of the Tanzanian Rift, East Africa, *Geophys. J. Int.,* **210**(1), 465–481.

Rasskazov, S.V., Logachev, N.A., Ivanov, A.V., Boven, A.A., Maslovskaya, M.N., Saranina, E.V., Brandt, I.S. & Brandt, S.B., 2003. A magmatic episode in the Western Rift of East Africa (19-17 Ma), *Geol. Geofiz.,* **44**(4), 317–324.

Roberts, E., O'Connor, P.M., Stevens, N.J., Gottfried, M.D., Jinnah, Z.A., Ngasala, S., Choh, A.M. & Armstrong, R.A., 2010. Sedimentology and depositional environments of the Red Sandstone Group, Rukwa Rift Basin, southwestern Tanzania: new insight into Cretaceous and Paleogene terrestrial ecosystems and tectonics in sub-equatorial Africa, *J. Afr. Earth Sci.,* **57,** 179–212.

Roberts, E., Stevens, N., O'Connor, P., Dirks, P., Gottfried, M., Clyde, W. & Hemming, S., 2012. Initiation of the western branch of the east African rift coeval with the eastern branch, *Nat. Geosci.,* **5**(4), 289–294.

Rudnick, R. & Fountain, D., 1995. Nature and composition of the continental-crust—a lower crustal perspective, *Rev. Geophys.,* **33**(3), 267–309.

Rudnick, R. & Gao, S., 2003. The role of lower crustal recycling in continent formation, *Geochim. Cosmochim. Acta.,* **67**(18), A403–A403.

Schlüter, T. & Hampton, C., 1997. *Geology of East Africa,* Borntraeger.

Shillington, D. *et al.*, 2016. Acquisition of a unique onshore/offshore geophysical and geochemical dataset in the northern Malawi (Nyassa) rift, *Seismol. Res. Lett.,* **87**.

Specht, T. & Roshedahl, B., 1989. Architecture of the Lake Malawi Rift, East Africa, *J. Afr. Earth Sci.,* **8,** 355–382.

Tarkov, A. & Vavakin, V., 1982. Poisson's ratio behaviour in various crystalline rocks: application to the study of the earth's interior, *Phys. Earth planet. Inter.,* **29**(1), 24–29.

Tugume, F., Nyblade, A. & Julia, J., 2012. Moho depths and Poisson's ratios of Precambrian crust in East Africa: evidence for similarities in Archean and Proterozoic crustal structure, *Earth planet. Sci. Lett.,* **355,** 73–81.

Van Wijk, J.W., Lawrence, J.F. & Driscoll, N.W., 2008. Formation of the transantarctic mountains related to extension of the West Antarctic Rift system, *Tectonophysics,* **458,** 117–126.

Wolbern, I., Rumpker, G., Schumann, A. & Muwanga, A., 2010. Crustal thinning beneath the Rwenzori region, Albertine rift, Uganda, from receiver-function analysis, *Int. J. Earth Sci.,* **99,** 1545–1557.

Zhu, L. & Kanamori, H., 2000. Moho depth variation in southern California from teleseismic receiver functions, *J. geophys. Res.: Solid Earth,* **105,** 2969–2980.

Zandt, G. & Ammon, C., 1995. Continental crust composition constrained by measurements of crustal Poission's ratio, *Nature,* **374,** 152–154.

SUPPORTING INFORMATION

Supplementary data are available at *GJI* online.
Supplement A
Supplement B
Supplement C
Please note: Oxford University Press is not responsible for the content or functionality of any supporting materials supplied by the authors. Any queries (other than missing material) should be directed to the corresponding author for the paper.

Downloaded from https://academic.oup.com/gji/article-abstract/215/2/1410/5068696 by Penn State University (Paterno Lib) user on 17 September 2018